Fault slip-rates and Coulomb stress interactions in the intersection zone of the Hope, Kelly and Alpine Faults, South Island, New Zealand

Jessie L. Vermeer [a,*], Mark C. Quigley [a], Robert M. Langridge [c], Brendan G. Duffy [a,b], Zoë K. Mildon [d], Manuel-Lukas Diercks [d]

[a] *University of Melbourne, School of Geography, Earth and Atmospheric Sciences, Parkville, Victoria 3010, Australia*
[b] *GHD Pty Ltd, 180 Lonsdale Street, Melbourne, Victoria 3000, Australia*
[c] *GNS Science, Lower Hutt, New Zealand*
[d] *University of Plymouth, Plymouth, Devon PL4 8AA, United Kingdom*

ARTICLE INFO

ABSTRACT

Plate boundary faulting in New Zealand's South Island involves transfer of ~50% of slip from the largest fault (Alpine Fault) onto the Hope-Kelly Fault system through a structurally complex fault intersection zone. The slip-rate contributions of faults within the Hope-Kelly system and possible role of static stresses in facilitating slip transfer are explored in this study. Lidar-based geomorphic and fault mapping combined with luminescence dating of fault-proximal sedimentary deposits constrain post-last glacial slip-rates on the Hope and Kelly faults. Dextral slip-rates on the central Hope Fault (12–15 mm/yr) decrease westward on the Taramakau section from 5.6 (+2.1/−0.7) mm/yr to 1.7 (+1.0/−0.5) mm/yr. Dextral slip-rates on the Kelly Fault range from 6.2 (+2.7/−1.0) mm/yr to 2.0 (+2.5/−0.7) mm/yr to 6.2 (+7.8/−1.4) mm/yr. Proposed causes of slip-rate spatial variations include (i) complex slip localization and transfer across the deformation zone, (ii) undocumented slip on obscured or unrecognized faults, and (iii) possible transience in slip behaviours. Paleoseismic trenching and radiocarbon ages constrain timing of most recent surface rupture on the western Hope Fault to ca. 1680–1840 CE, with a preferred age of ca. 1800–1840 CE. Coulomb fault stress modelling indicates central Alpine Fault ruptures impart positive stress changes on Hope-Kelly receiver faults >5–10 bars, while Northern Alpine Fault earthquakes reduce Coulomb stresses on Hope-Kelly receiver faults, and vice versa. These results suggest central Alpine Fault earthquakes may propagate onto or trigger ruptures of Hope-Kelly Faults, but Hope-Kelly ruptures reduce stress on the northern Alpine Fault, possibly making ruptures of that fault less likely. This system of stress perturbations provides a mechanism for slip transfer from the central Alpine Fault onto the Hope Fault system.

1. Introduction

Fault slip-rates are important parameters in evaluating earthquake spatio-temporal patterns (e.g., Langridge et al., 2017; Elliott et al., 2018; Zinke et al., 2019; Zinke et al., 2021; Hatem et al., 2020) and undertaking probabilistic seismic hazard and fault displacement hazard analyses (e.g., Stirling et al., 2012; Moss and Ross, 2011). Continental plate boundaries commonly include hierarchical networks of large, fast-slipping (>10 mm/yr) faults and secondary, slower-slipping (ca. 1–10 mm/yr) faults that interact structurally and kinematically to accommodate tectonic strain. Faults may exhibit significant slip-rate temporal variations (Gold and Cowgill, 2011) that reflect a variety of factors including stress shadowing (e.g. Nicol et al., 2006; Khajavi et al., 2018;

Ninis et al., 2013; Gauriau and Dolan, 2021), temporal changes in fault strength (e.g. Dolan et al., 2016), and temporal earthquake clustering (e. g. Rockwell et al., 2000; Dolan et al., 2007). Derivation of fault slip-rates, faulting kinematics, and earthquake chronologies across diverse time-scales provide opportunities to advance our understanding of the nature and mechanics of fault interactions in plate boundaries.

The geometric connectivity of interacting faults within a fault network can impart important controls on how slip is transferred through the fault system in individual earthquakes (i.e., coseismic rupture propagation) and over geological time-scales incorporating many diverse earthquake scenarios (e.g., Parsons et al., 2012; Quigley et al., 2019). Although the timing of earthquakes on individual faults inferred from paleoseismic data may be used to investigate earthquake

---

spatial-temporal clustering via fault interaction, for fast-slipping faults with short recurrence intervals, it may often be difficult to discriminate between clustered events with a common underlying causal mechanism from random earthquake events, particularly if the timing of past earthquakes is not precisely constrained. This is important to resolve in seismic hazard analysis because (i) co-seismic rupture propagation across many faults can increase the moment magnitude (Mw) of the earthquake and (ii) stress transfer across diverse faults in a network may influence the subsequent hazard following a major earthquake, and the longer-term hazard associated with fault slip-rate variability. Modelling of Coulomb stress changes imparted by earthquake source faults on receiver faults within a fault network can provide important insights into how the structure of a fault network may promote or inhibit various rupture scenarios among proximate faults (e.g., Parsons et al., 2012; Quigley et al., 2019; Mohammadi et al., 2019).

The Marlborough Fault System (MFS) in the northern South Island (Fig. 1) consists of a series of large dextral strike-slip faults and interspersed secondary faults that transfer plate boundary strain from the Hikurangi subduction zone through to the Alpine Fault (Barnes and Audru, 1999; Norris and Cooper, 2001; Van Dissen and Yeats, 1991; Langridge et al., 2010; Langridge et al., 2003; Yang, 1991; Khajavi et al., 2016; Cowan and McGlone, 1991; Cowan, 1990; Khajavi et al., 2018; Langridge et al., 2003). This study focuses on a particularly complex region of the MFS, where the southernmost and fastest-slipping fault in the MFS (Hope Fault, 12–23 mm/yr, see references in Fig. 1) diverges from a principal fault trace into several interacting splay faults (the Hope-Kelly Fault system; Vermeer et al., 2021) as it interacts with the Alpine Fault. The primary objective is to obtain new fault slip-rate data from this sparsely-studied area of the MFS to compare with emerging datasets from other parts of the MFS (Khajavi et al., 2018; Hatem et al., 2020; Zinke et al., 2021) and the Alpine Fault (Langridge et al., 2017; Howarth et al., 2018, 2021) to enhance our understanding of the rates
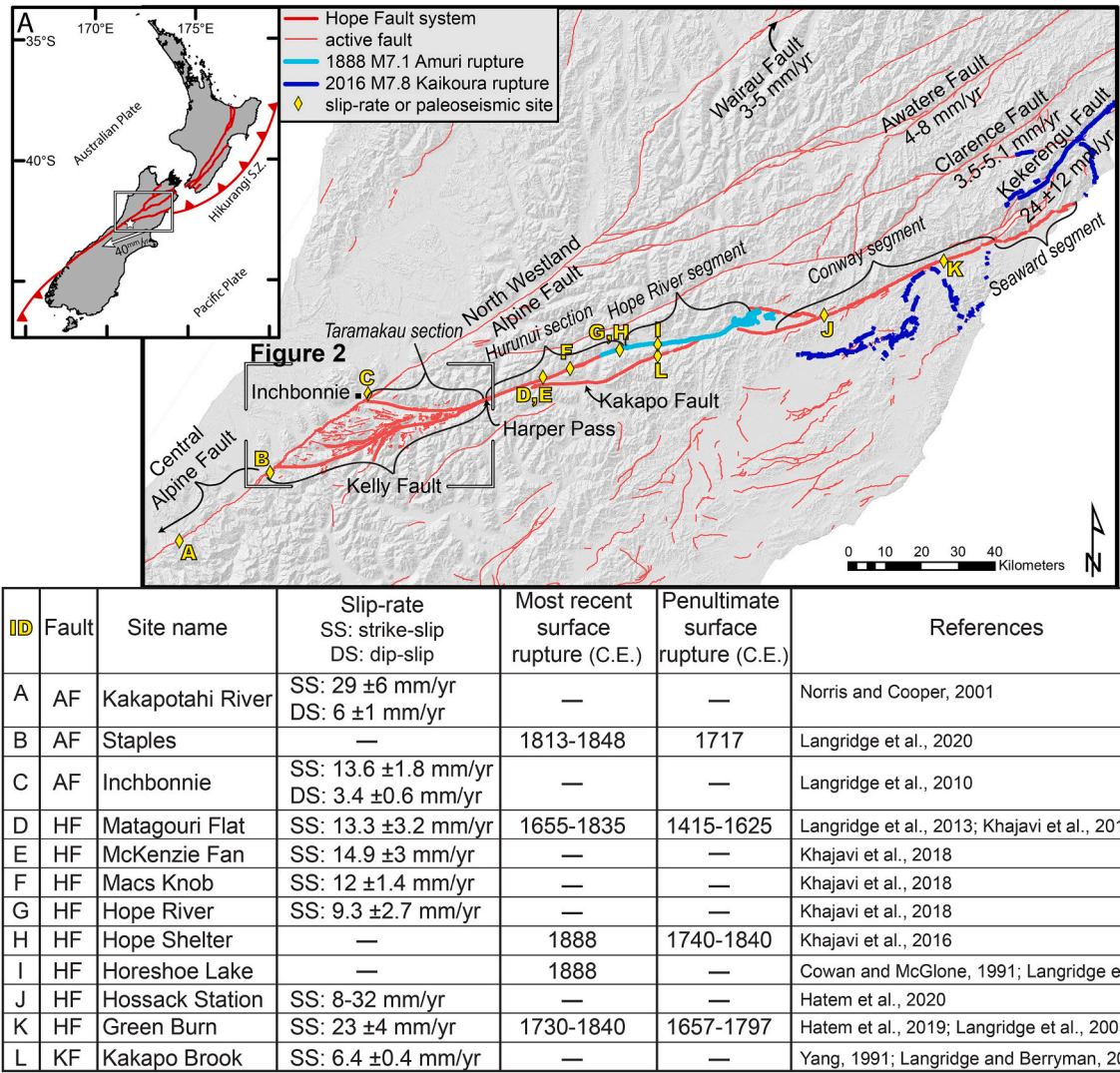

ID	Fault	Site name	Slip-rate SS: strike-slip DS: dip-slip	Most recent surface rupture (C.E.)	Penultimate surface rupture (C.E.)	References
A	AF	Kakapotahi River	SS: 29 ±6 mm/yr DS: 6 ±1 mm/yr	—	—	Norris and Cooper, 2001
B	AF	Staples	—	1813-1848	1717	Langridge et al., 2020
C	AF	Inchbonnie	SS: 13.6 ±1.8 mm/yr DS: 3.4 ±0.6 mm/yr	—	—	Langridge et al., 2010
D	HF	Matagouri Flat	SS: 13.3 ±3.2 mm/yr	1655-1835	1415-1625	Langridge et al., 2013; Khajavi et al., 2018
E	HF	McKenzie Fan	SS: 14.9 ±3 mm/yr	—	—	Khajavi et al., 2018
F	HF	Macs Knob	SS: 12 ±1.4 mm/yr	—	—	Khajavi et al., 2018
G	HF	Hope River	SS: 9.3 ±2.7 mm/yr	—	—	Khajavi et al., 2018
H	HF	Hope Shelter	—	1888	1740-1840	Khajavi et al., 2016
I	HF	Horeshoe Lake	—	1888	—	Cowan and McGlone, 1991; Langridge et al., 2013
J	HF	Hossack Station	SS: 8-32 mm/yr	—	—	Hatem et al., 2020
K	HF	Green Burn	SS: 23 ±4 mm/yr	1730-1840	1657-1797	Hatem et al., 2019; Langridge et al., 2003
L	KF	Kakapo Brook	SS: 6.4 ±0.4 mm/yr	—	—	Yang, 1991; Langridge and Berryman, 2005

Fig. 1. A) Tectonic setting of New Zealand. The white arrow shows the Australian-Pacific relative plate motion at the Hope-Kelly-Alpine fault intersection. B) Active faults of the northern South Island, including the Alpine fault and Marlborough fault system, with generalized slip rates of the Clarence, Awatere, Wairau, and Kekerengu faults (Little et al., 2018; Maon, 2006; Zachariasen et al., 2006; Nicol and Van Dissen, 2002). The Hope fault system is shown in bold red, with segments labelled in black and historic surface rupture extents highlighted in blue and light blue (1888 Amuri earthquake, 2016 Kaikoura earthquake, respectively). Yellow diamonds and letters indicate slip-rate or paleoseismic study sites, and the letters correlate to ID in the table which shows the measured slip-rate and/or dates of most recent and penultimate surface rupture, with references (Cowan and McGlone, 1991; Norris and Cooper, 2001; Yang, 1991; Langridge et al., 2003; Langridge et al., 2010; Langridge et al., 2014; Khajavi et al., 2016; Khajavi et al., 2018; Hatem et al., 2020; Hatem et al., 2020; Langridge et al., 2020). The Fault column refers to the fault on which the slip-rate is measured, AF - Alpine fault, HF - Hope fault, KF – Kakapo fault. This figure does not include new slip-rates presented in this study. The white corner marks show the extent of Fig. 2. (For interpretation of the references to colour in this figure legend, the reader is referred to the web version of this article.)

and kinematics of late Quaternary faulting in this region. Using a combined approach of structural-geomorphic mapping, dating of fault-associated sediments and landforms, and Coulomb stress modelling scenarios, we characterize earthquake behaviours and fault interactions in this incipient plate boundary fault interaction zone. The results are relevant to understanding seismic hazard (Stirling et al., 2012) and faulting in this region (e.g., Litchfield et al., 2014; Langridge et al., 2016) and analogous regions globally.

2. Geologic setting

The Alpine Fault and the Marlborough Fault System (MFS) dextral strike-slip fault zones accommodate approximately 80% of the total relative Australian-Pacific plate velocity in the northern South Island of New Zealand (Fig. 1; Barth et al., 2013; Norris and Cooper, 2001; Sutherland et al., 2007; Wallace et al., 2007; Howarth et al., 2018). The Alpine Fault is a dextral-reverse fault with a straight surface trace and moderate to shallow SE dip (Barth et al., 2013; Berryman et al., 1992; Norris and Cooper, 2001; Howarth et al., 2018). Slip-rates vary along its length. The central section has a maximum of 28 ± 4 mm/yr dextral and up to >12 mm/yr of reverse slip and northern section has a slip-rate that decreases from 14 ± 2 mm/yr at the southern end to 10 ± 2 mm/yr at the northern end (Norris and Cooper, 2001; Langridge et al., 2010; Langridge et al., 2017; Howarth et al., 2018). The Hope Fault is the southernmost fault in the MFS. It extends from the central-northern section boundary of the Alpine Fault to the NE coast of the South Island where it interacts with the Hikurangi subduction zone (Nicol and Van Dissen, 2002; Langridge et al., 2003; Barth et al., 2013). The ENE-striking Hope Fault is primarily dextral slip and is divided into five geometric segments with two branching faults (the Kakapo and the Kelly) and one large stepover (Hanmer Basin) (Fig. 1) (Freund, 1971; Langridge et al., 2003). The slip-rate varies along the fault (Fig. 1 and references therein). Balancing the horizontal slip vector shows that the central Hope Fault (Hurunui segment plus Kakapo fault) accommodates the same amount and direction of slip as the decrease on Alpine Fault at the central-northern transition (Langridge et al., 2010). The slip transfers between the Alpine and Hope Faults via the Hope-Kelly Fault system, made of the Taramakau section of the Hope Fault, the branching Kelly Fault, and all intervening faults. The Hope-Kelly Fault system is a horsetail-like structure of north dipping dextral-normal oblique faults and south dipping normal faults that abut the Alpine Fault on the west side and converge eastward into the narrow dextral fault zone of the central Hope Fault (Vermeer et al., 2021).

The rupture record of the Alpine Fault is well known from on- and off-fault paleoseismic studies (De Pascale et al., 2014; Howarth et al., 2018 and studies therein), that define a recurrence interval of <300 years (Howarth et al., 2021; Cochran et al., 2017). Nevertheless, the Alpine Fault has not had a historic surface rupture (i.e., since c. 1840 CE). Paleoseismic studies indicate that in about 1717 CE the Alpine Fault hosted a very large to great (M > 8) earthquake that ruptured the southern, central, and part of the northern segment (Wells et al., 1999; Howarth et al., 2018). At the central-northern section boundary a more recent faulting event has been identified as occurring in 1813–1840, shortly before the historic period (Langridge et al., 2020). This event is co-temporal with a turbidite in Lake Kaniere (Howarth et al., 2021), but not in Lake Brunner or lakes to the south, suggesting that this earthquake may have involved only a small length of the Alpine Fault.

The Hope Fault has had one historic surface rupturing earthquake, the Mw ~7.1 Amuri earthquake in 1888 CE, the extent of which is shown in Fig. 1 (McKay, 1890; Khajavi et al., 2016). The eastern sections of the Hope Fault did not have surface rupture in the 2016 Kaikoura earthquake (Litchfield et al., 2018). The dates of the most recent surface rupture and the penultimate surface rupture at paleoseismic sites on the Hope Fault to date are shown in Fig. 1. There has been no previous paleoseismic data for the Taramakau section or the Kelly Fault.

Vermeer et al. (2021) recently studied the Hope and Kelly faults west

of the Main Divide using lidar and field mapping of surrounding landforms. They identified sections of principal slip zones along the faults, where individual fault traces have accumulated displacement from multiple surface ruptures. In this study, we examine some of these fault scarps in more detail, present optically stimulated luminescence (OSL) and radiocarbon ages for some landforms from hand-dug pits and outcrops, conduct paleoseismic investigations, and determine slip-rates.

With relevance to the age and origin of geomorphic features in the study area, the most recent glacial period in New Zealand (Otiran) occurred during marine isotope stage (MIS) 2 to 4 with up to 8 glacial advances identified during that time (Shulmeister et al., 2019). The Taramakau glacier had three advances during the glacial interval 26–17 ka (Barrell et al., 2011; Barrows et al., 2013). The oldest MIS-2 advance of the Taramakau glacier is 24.9 ± 0.8 ka (Fig. 2 Kumara-2_1 advance, Loopline Formation moraine, Barrell et al., 2011; Barrows et al., 2013). East of the Main Divide, downvalley glacial deposits in the Waimakariri River Valley are as old as 26 ka (Rother et al., 2015), indicating the upper parts of the Taramakau Valley were probably also glaciated by that time. The Kumara-2_1 advance was followed by a short recession with an unknown amount of glacial retreat, and a readvance at 20.8–20 ka (Fig. 2 Kumara-2_2 advance, Larrikins Formation moraine, Barrell et al., 2011; Barrows et al., 2013). Glaciofluvial sediments in the Rangitata valley (20–26 ka, Shulmeister et al., 2018), fluvial sand in Otago (24.8 ± 2.7 ka, Stahl et al., 2016), outwash sediments in the Grey River valley (21.3–23.9 ka, Hormes et al., 2003), and alluvial sediments in the Hope River valley (23.9 ± 1.5 ka, Khajavi et al., 2016), indicating a regional pulse of outwash/alluvial sedimentation between the 26–24 ka advance and the ~20 ka advance in catchments surrounding the Taramakau River. The latest ice deposited features on the coastal plain are Moana Formation moraines (Kumara-3, Barrell et al., 2011; Barrows et al., 2013), dated at 17.3 ± 0.5 ka at Lake Brunner, indicating at that time the Taramakau River valley and tributary catchments (Otira and Otehake rivers) were fully glaciated. End moraines at Arthurs Pass are 15.2 ± 0.8 ka (Eaves et al., 2017), indicating that at this time the lower elevations were free of glacial ice. The sites of interest in this study are all well below the elevation of the Arthurs Pass end moraines, so by inference they were ice-free before 15.2 ± 0.8 ka. Thus, the last deglaciation of the Taramakau River valley occurred no earlier than 17.3 ± 0.5 ka and was complete by 15.2 ± 0.8 ka.

3. Methods

3.1. Lidar and field-based fault analysis

Faulted geomorphic features with similar morphology, position, trend, and relative age (inferred from elevation and terrace-sequence interpretations) were mapped in lidar-derived bare-earth DEMs (e.g., Vermeer et al., 2021) and correlated across fault traces (Lidar collection details are in Appendix A). Detailed geomorphic mapping and field observations of stratigraphy, combined with absolute age control (see below) were used to determine the sequence of events which produced the present geomorphology of each site. Geomorphic surfaces were numbered in the order of formation, so the oldest identified surface is "1" and the numbers increase with decreasing age. Lateral displacements were measured parallel to the fault trace orientation in map view on lidar using linear features such as terrace riser tops or stream channels (e.g., Cowgill, 2007; Zielke et al., 2015; Khajavi et al., 2016; Mackenzie and Elliott, 2017; Zinke et al., 2017; Khajavi et al., 2018; Zielke, 2018; Zinke et al., 2021). Minimum (maximum) displacements are considered the minimum (maximum) feasible distances between offset features projected to the fault trace. Preferred displacements represent our expert consensus on most likely offsets. We do not consider distributed deformation around the fault trace (e.g. Kearse et al., 2018; Quigley et al., 2012) due to a paucity of linearly correlative structures that could be reliably used to estimate broader wavelength deformation.

Vertical displacements were measured using a combination of scarp-
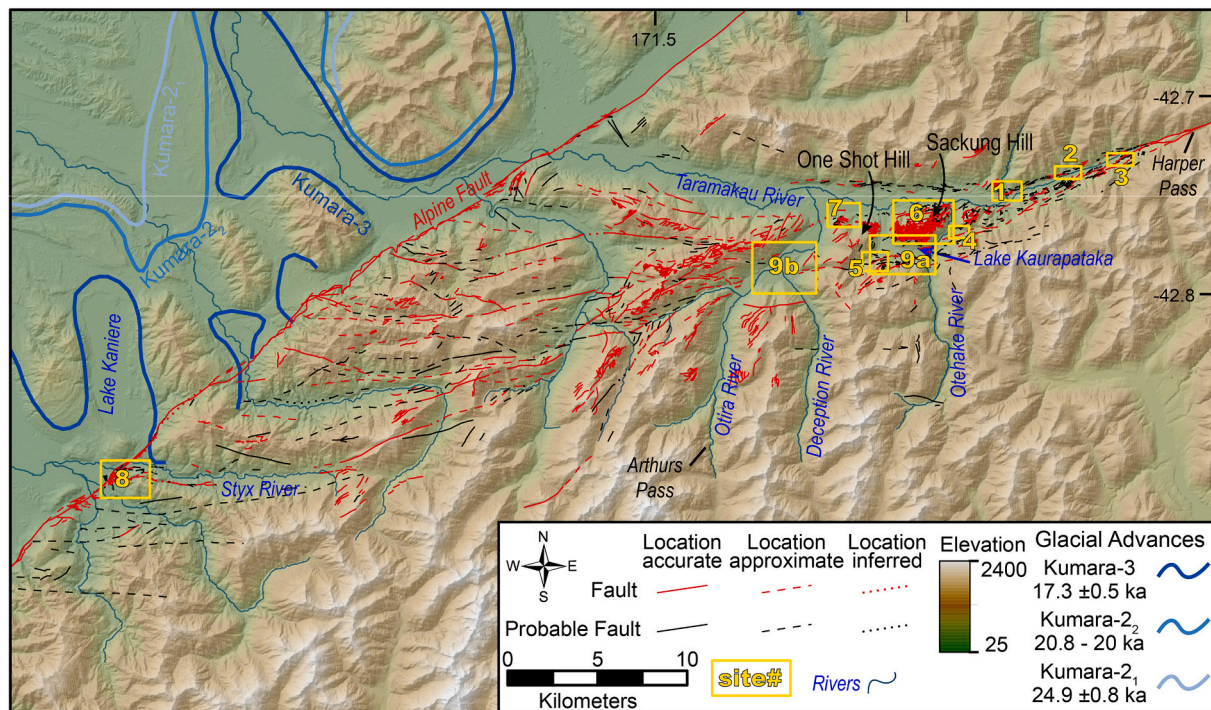
Fig. 2. Map of the study area, showing topography and active faults from Harper Pass and Arthurs Pass to the coastal plain. The extent of sites in this study are shown with yellow boxes. Significant rivers are labelled in blue. The maximum extent of recent glaciations are shown in shades of blue and labelled (Barrows et al., 2013), approximate ages of each maximum are shown in the legend (Barrell et al., 2011; Barrows et al., 2013). (For interpretation of the references to colour in this figure legend, the reader is referred to the web version of this article.)

perpendicular and scarp parallel topographic profiles to match geomorphic surfaces and features across the fault (e.g. Khajavi et al., 2016). The fault parallel profiles were used to evaluate how the landforms match on either side of the fault and to determine the present elevations of correlative features. Some fault parallel profiles are set back from the fault trace to avoid scarp degradation and deposition that could alter the original morphology of pre-faulting landforms. On sloped landscapes, the horizontal distance between fault parallel profiles results in elevation difference between the profiles that is unrelated to faulting and that must be accounted for in analysis of vertical displacements. Fault-perpendicular topographic profiles were used to determine the pre-faulting landform slope and calculate the expected pre-faulting vertical offset of the feature and the scarp parallel profiles. Landforms were projected across the fault onto an approximation of the fault plane with an interpreted range of dip (e.g. dip of $80 \pm 10°$ N). Fault parallel profiles were also used to estimate fault displacement by restoring elevation differences associated with lateral offsets of variable slope topography and measuring the residual (vertical faulting-related) displacement. All lidar-derived displacement measurements were ground-truthed in the field. Additional field investigations included hand-dug excavation of a trench across the fault (Fig. 2 site 1) where we identified a discrete fault scarp offsetting alluvial fan sediments adjacent to a swamp in the lidar, and investigations of faulted stratigraphy in natural exposures and hand-dug sample pits.

3.2. OSL, IRSL and radiocarbon (14C) dating of fault-proximate sediments

Prior studies utilizing OSL and IRSL to estimate the ages of Quaternary sediments in New Zealand's South Island include Hormes et al. (2003), Sohbati et al. (2016), Khajavi et al. (2016), Shulmeister et al. (2018), Rother (2006), Rother et al. (2010), Rowan et al. (2012), Stahl et al. (2016) and Zinke et al. (2017). OSL and IRSL samples in the study area were obtained from excavated and cleaned outcrops, trench walls,

and pits. Samples were analysed by the Nordic Laboratory for Luminescence Dating at Aarhus University and DTU Physics in Denmark, following the method of Sohbati et al. (2016) for quartz OSL, and feldspar IR50 and pIRIR. Because it is the most readily bleached (Sohbati et al., 2016), the quartz OSL age is used as the absolute age for the sediment deposition. The ratio between the quartz OSL age and the age from two components of feldspar IRSL (pIRIR, IR_{50}) was used to evaluate the likelihood that the quartz grains were well-bleached during the last depositional event (Sohbati et al., 2016; Murray et al., 2012). The quartz OSL is considered very likely bleached during the most recent deposition if $IR_{50}/OSL \leq 1$ and $pIRIR/OSL \approx 1$. If one or both of these conditions are not met, the OSL age may or may not have been completely reset during the most recent deposition; this does not invalidate the OSL age, but it must be applied with caution. Additional information pertaining to the background and theoretical framework for the OSL and IRSL dating undertaken here is presented in Appendix A.

Radiocarbon samples ($14C$) were selected from organic material in sediments and analysed at the GNS Science Rafter Radiocarbon Lab in New Zealand. We selected samples with a preference for material that is clearly detrital, such as seeds, leaves or charcoal. Charcoal may have significant inherited age, making it less desirable than seeds or leaves (Howarth et al., 2018). Twigs may be detrital but may not be readily distinguishable from rootlets that could be significantly younger than the age of the sediment. Bioturbation by burrowing animals or plant roots can potentially emplace younger organic material into a sediment after deposition. Age determinations used the Southern Hemisphere calibration model of Hogg et al. (2020). Sample information, including description of material and analysis details, are presented in Appendix B.

3.3. Slip-rate calculations

Slip-rates were estimated using displacements, relative geomorphic ages, and absolute ages from OSL. We used @RISK to conduct Monte Carlo simulations that take into account a defined probability

distribution (PDF) for each source of identified uncertainty, including the age, displacement, and fault orientation (e.g. Zechar and Frankel, 2009). The probability distribution was chosen according to the characteristics of the value, for instance displacement measurements were often represented by a PERT (continuous probability distribution defined by a minimum, maximum and preferred value) or triangular distribution with the minimum and maximum displacement values representing the 95% confidence interval of the distribution and the
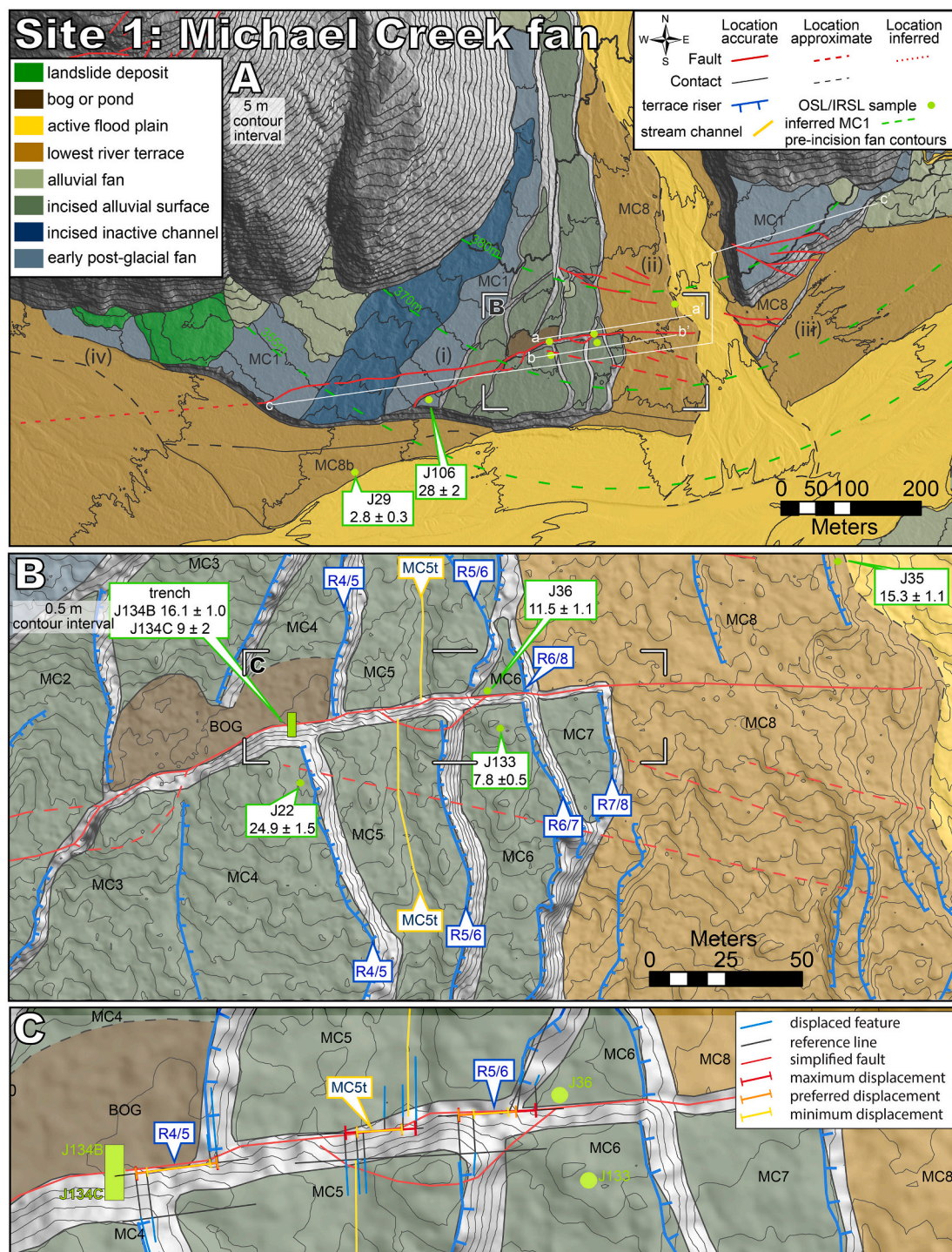
Fig. 3. Geomorphic map of Site 1: Michael Creek with sample locations and luminescence or 14C ages. A) White lines show the locations of topographic profiles in Fig. 5 (a-a' and b-b') and Fig. 6 (c-c'). Green lines show the inferred topographic contours of the earliest postglacial fan, of which the MC1 surfaces are remnants. Numerals indicate locations of interest referred to in the text. Contour interval is 5 m. B) Locations of OSL samples shown with green dots, OSL sample ages are in green boxes, trench is green rectangle. Surfaces are labelled (MCx), terrace risers (Rx/x), and the channel on MC5 (MC5t). Contour interval is 0.5 m. The extent of panel C is shown by the white corner marks. C) Displacement measurements used in slip-rate calculations (R4/5, MC5t, R5/6), showing minimum, maximum, and preferred displacement measurements. Reference lines and simplified fault show the top and base of fault scarp, and projection of the displaced features across the scarp. Displaced feature lines show the range of position used for features that have a diffuse shape. (For interpretation of the references to colour in this figure legend, the reader is referred to the web version of this article.)

peak at the preferred measurement. OSL and IRSL ages are represented by a normal distribution with the mean and standard deviation defined by the age and standard error returned from the lab. The @RISK slip-rate calculation sheet, variable PDFs and final slip-rate values and distributions are presented in Appendix C.

3.4. Coulomb stress modelling

To investigate co-seismic stress transfer and rupture behaviours for a variety of earthquake scenarios on the Hope, Kelly and/or Alpine Faults, we built a discretized 3D fault model (using methods outlined in Mildon et al., 2016 and Hughes et al., 2020) and undertook Coulomb stress transfer analysis (e.g., King et al., 1994; Stein et al., 1997; Toda et al., 1998; Harris et al., 1995) using Coulomb 3.4 (Toda et al., 2005; see https://github.com/ZoeMildon/3D-faults). Relevant Coulomb stress theory and details pertaining to the fault model construction and stress analysis are provided in Appendix A.

4. Results: geomorphic mapping, displacements, slip-rates, earthquake chronologies

4.1. Site 1 Michael Creek fan

4.1.1. Geomorphic mapping

On the Hope Fault, we identified a suite of faulted and progressively displaced terraces at Michael Creek, a tributary that enters the Taramakau River from the north (Fig. 3). This site is at a major bend in the Taramakau River valley (Fig. 2 Site 1). East and upstream of this site, the Taramakau River valley trends ~070°, parallel to the Hope Fault, and west of this site the valley bends to ~090°. The Hope Fault is inferred to also bend and follow this trend, though no surface expression of the Hope Fault has been identified west of the Michael Creek fan (Vermeer et al., 2021). The Hope Fault is proposed to become an oblique extensional fault to the west, while most of the strike-slip motion is transferred south onto the Kelly Fault via NNE-striking linking faults (Vermeer et al., 2021).

On the west side of the Michael Creek active channel, the main fault trace splits into two traces on the west side of the fan (Fig. 3A, location i). The fault is south side up, with small pop-ups on the south side. On the west side of the fan where the fault has two traces (Fig. 3A location i) the terrace risers are oblique to the fault and displacements are smaller on each fault splay. Secondary faults interpreted as Riedel faults extend north and possibly south from the main fault (Fig. 3A location ii). East of the active creek, the fault is only well defined on the highest surface (MC1), where it has 4 splays in a horsetail formation. The fault likely also cuts the lower eastern terraces (MC8, Fig. 3 location iii), but the scarps, if present, are poorly defined.

The Michael Creek fan has a suite of 8 alluvial surfaces. East of the creek, only the oldest (MC1) and youngest (MC8) surfaces are preserved. West of the creek, the entire suite is preserved and progressively displaced by the main trace of the fault. Surface MC5 has a distinctive preserved channel (MC5t) that matches across the fault with high confidence. The high confidence cross-fault correlation of MC5 is a marker for the correlation of surfaces relatively older and younger. Surfaces MC4 and MC3 and the riser between them is obscured north of the fault by a fault-bounded peat bog/swamp. South of the fault, surface MC7 is preserved, but the correlative surface north of the fault is not preserved; we attribute this to the uplift of the south side relative to the north side. Besides MC7, all other surfaces are preserved both north and south of the fault. The youngest surface, MC8, is barely displaced by the fault, with only a small scarp (< 10 cm) that can be identified in the field but a confident displacement measurement cannot be made because the fluvial/alluvial surface features are of similar ~10 cm magnitude. More details of the geomorphic mapping and observations are included in Appendix D.

4.1.2. Trench (J134)

We hand-dug a trench across the Hope Fault at location J134 (Fig. 3B, Fig. 4). The trench exposed cobble gravel with a reddish-brown matrix north of the fault (unit RS, Fig. 4), and grey pebbly silt south of the fault (unit GS, Fig. 4). The fault zone was distinguished by a zone of mixed particles of sediment from either side of the fault (unit FF, Fig. 4), the south edge of the fault zone strikes 082° and dips 62° S. Overlying the fault zone is a package of unfaulted colluvial sediment (unit TC, Fig. 4). At contact between RS, TC and FF in the central/south part of the trench, part of unit TC is beneath RS, which we interpret as TC infilling a pocket/irregularity in the surface topography formed by the most recent surface rupture (Fig. 4 picture). P. Because TC appears unfaulted and is not mixed into FF, we interpret it as a post-faulting unit. A more detailed description of the trench observations is presented in Appendix D.

Unit GS was sampled for 14C and OSL, RS for OSL and TC for 14C. The TC 14C material (sample J134D) comprised small twigs or roots that yield modern ages (Fig. 4). These may be in-grown roots that post-date the sediment or the sediment might be modern in age. Unit RS yielded an OSL age of 9 ± 2 ka (Sample J134C, Table 1). The significance of this age in the geomorphic development of the Michael Creek fan is discussed in Section 4.1.3.

The GS 14C material (sample J134A; small bark fragments) yields an age of 242 ± 19 radiocarbon years (Fig. 4 inset 14C calibrated age curve). Its calibrated age range is 1653–1677 (22.5%) or 1735–1800 (73.0%) Cal CE. Because unit GS has little to no evidence of root growth or bioturbation, and the sediment is tightly packed and seems to have little pore space or pore connectivity, the bark is interpreted as being incorporated into the sediment during deposition and thus represents a maximum depositional age for unit GS. Heavily abraded organic fragments may have an inherited age component relative to the timing of the sediment deposition, so 1653 CE is considered a maximum depositional age for the sediment. Because this unit is faulted, at least one surface rupture has occurred on this fault since the deposition of unit GS, with a maximum age of 1653 CE. The minimum age of the most recent surface rupture could potentially be as young as 1848 CE, after which a surface rupturing earthquake would be expected to have been historically recorded (Langridge et al., 2020).

Unit GS yielded an OSL age of 16.1 ± 1.0 ka (sample J134B, Table 1). This age is substantively older than the 14C sample from the same unit. The possibility of short transport distances, transport occurring at night and/or in a rapid transport and deposition event (e.g. debris flow or flood event), and/or high turbidity and suspended load during fluvial transport that attenuated light and blocked the grains in the lower water column from being bleached (Brown, 2020) are possible mechanisms whereby the OSL age could be significantly older than the sediment depositional age. Because it is unlikely that the 14C dated material was incorporated into the sediment after deposition (see previous paragraph), but we cannot rule out the possibility of inherited OSL age, we consider the 14C age (sample J134A, 1653–1800 CE) to most closely represent the depositional age of this sediment.

4.1.3. Stratigraphy and OSL/IRSL samples

We hand dug pits to observe the physical characteristics of the terrace sediments and collect samples for dating. The locations of luminescence samples are in Fig. 3. Stratigraphic logs, description of the sampling pits/outcrops, and photos are in Fig. 5. We observed some similarities in physical characteristics of the sediments across the pits and have identified clusters of luminescence ages that we used to estimate absolute ages of geomorphic and sedimentological features and events.

J106 and J22, on MC1 and MC4, had similar stratigraphy of an organic rich soil, overlying a lilac-grey coloured clay rich gravel horizon, over pebble to cobble gravel, with red-orange clay rich matrix and cobbles with up to 1 cm weathering rinds. The OSL samples taken from within this deeply weathered cobble gravel at J106 and J22 are 28 ± 2 ka and 24.9 ± 1.5 ka respectively. The pIRIR/OSL ratio and IR50/OSL
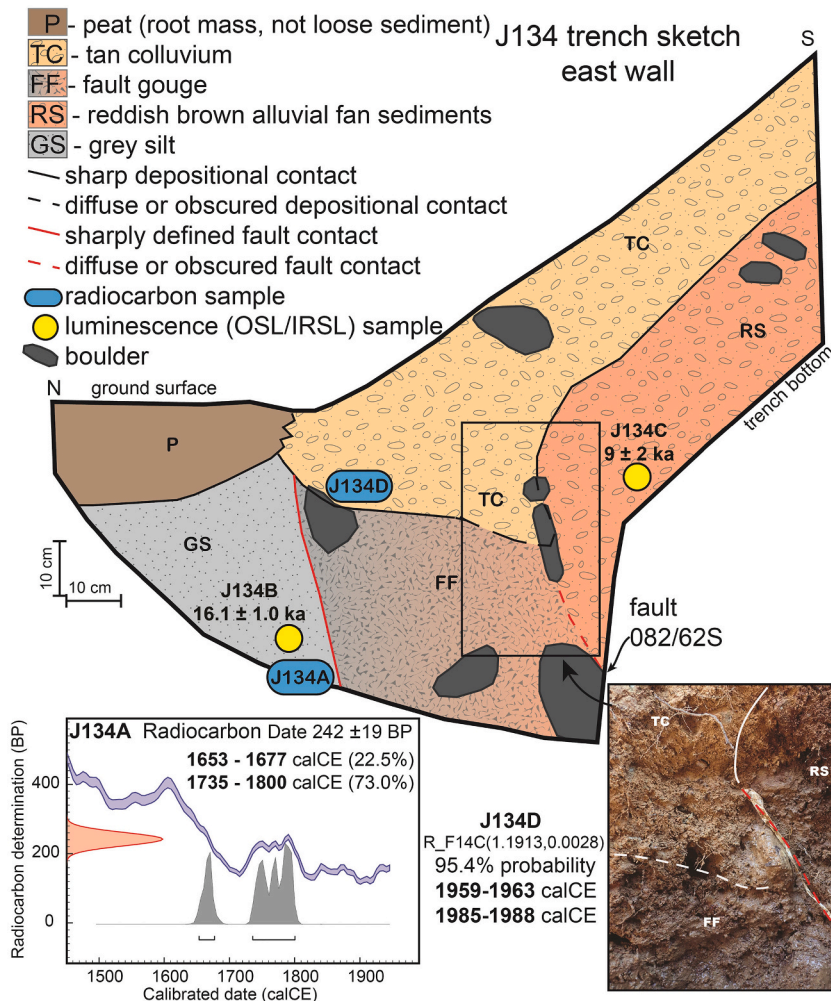
Fig. 4. Log of the east side of the Michael Creek fan hand-dug trench. OSL samples are shown by yellow circles, radiocarbon samples are shown by blue ovals. The trench reveals a ~ 30 cm wide fault zone between two lithologicaly distinct units, RS and GS, with peat (P) and colluvial sediment (TC) overlying the faulted sediments. The photo shows the complex triple contact between RS, TC and the fault (FF) where TC has infilled post-rupture topographic irregularities. The south edge of the fault zone is oriented 082/62S. The 14C calibration curve and resulting calibrated age (1653–1800 CE) for sample J124A is also shown (OxCal v4.4.4Bronk Ramsey, 2009; Atmospheric data from Hogg et al., 2020). 14C sample J134D returned a modern age. The locations of OSL samples J134C (9 ± 2 ka) and J134B (16.1 ± 1.0 ka) are also shown. (For interpretation of the references to colour in this figure legend, the reader is referred to the web version of this article.)

ratio indicate that J106 is well bleached and J22 is likely well bleached (see Appendix X). We observed similar sediment in the base of the pit at J36 on MC6, but did not sample that sediment for luminescence. The OSL age of these samples and the deep weathering led us to interpret these sediments as pre-last-glacial sediment that was not scoured out during the most recent glacial advance(s) (see 2. Geological Setting). At this low elevation near the valley floor, we consider it unlikely that any geomorphic surfaces would have survived glaciation, so these sediment ages are unrelated to the formation ages of the MC1 and MC4 surfaces and associated fault displacements.

Samples J35 (15.3 ± 1.1 ka), J36 (11.5 ± 1.0 ka), and J134B (16.1 ± 1.0 ka) are from slightly weathered sediments on the north side of the fault. Sample J35 is from a sandy lens in a sandy cobble gravel ~90 cm below the surface of the MC8 surface exposed in the cut of the active creek channel. Sample J36 is from a ~ 20 cm thick bluish grey silt on surface MC6. Sample J134B (16.1 ± 1.0 ka) is from the grey pebbly silt on the north side of the fault exposed in the trench beneath/adjacent to the peat bog that overlies surface MC4. For J35 and J36, the IR50/OSL ratio is ~1, but the pIRIR/OSL ratio is >1, meaning these samples likely have bleached quartz. Sample J134B has IR50 and pIRIR ages much older than the OSL age (IR50/OSL > 1 and pIRIR/OSL > 1), leaving uncertainty about whether the quartz in this sample was fully bleached, so the OSL age may be older than the last deposition. We interpret these sediments as postglacial material that was deposited as the last ice retreated and formed the MC1 fan. These sediments may or may not have been reworked during incision of the MC2–8 surfaces, but they retain the early post-glacial depositional age.

At J134C and J133 (Fig. 3 and Fig. 4 and Fig. 5) the sediment is moderately weathered gravel (clast weathering rinds <10 mm and mostly <5 mm) with a moderate amount of clay in the matrix. Sample J134C was taken from unit RS on the upthrown south side of the fault in the trench and yielded an OSL age of 9 ± 2 ka (Fig. 4 and Table 1). J133 was taken from the root ball of a fallen tree on MC6, which would have placed the sample at 1–1.5 m depth until the tree fell. The tree had fallen recently, shown by the mix of dead and live leaves both on the tree and on the surrounding damaged vegetation. J133 yielded an OSL age of 7.8 ± 0.5 ka (Table 1). Both J134C and J133 have IR50/OSL >1 and pIRIR/OSL >1, so We cannot be sure the OSL was completely bleached during deposition and may have inherited age.

Sample J29 is from a light grey sandy silt unit overlying a medium brown cobble gravel, representing deposition of/on MC8b. The OSL age of J29 is 2.8 ± 0.3 ka (Fig. 5 and Table 1).

4.1.4. Slip-rate

On the Michael Creek fan (Fig. 3), there are three terrace risers (R4/5, R5/6, R6/7) and one terrace tread channel (MC5t) that can be correlated across the fault. R4/5 has 9.4–12.1 m of displacement (maximum = preferred). The south-side-up vertical displacement is 2.0–2.3 m (maximum = preferred). R5/6 has 8.5 (+2.9/−3.3) m right-lateral displacement and vertical displacement is south-side up 1.3–2 m (minimum = preferred). Channel MC5t has lateral displacement is 6.7 (+3.8/−3.6) m, and south-side up vertical displacement of 2.0 m. The OSL sample J134C (9 ± 2 ka) constrains the formation age of MC4 by representing when the surface was active, and the sediment was

Table 1
Luminescence ages. Yellow shading indicates samples that are probably well bleached, based on the IR_{50}/OSL age ratio being ≤1. Green shading indicates sample that is well bleached, based on IR_{50}/OSL ratio being ≤1 and the pIRIR/OSL ratio being ~1. The OSL dose rate and radionuclide data table is in Appendix B.

Lab. Code	Sample	Site	Depth,	w.c.	IR_{50} D_e	(n)	pIRIR D_e	(n)	OSL D_e	(n)	feldspar dose rate,	quartz dose rate,	IR_{50} age,	pIRIR age,	**OSL age,**	IR_{50}/OSL	pIRIR/OSL
			cm	%	Gy		Gy		Gy		Gy/ka	Gy/ka	ka	ka	**ka**	age ratio	age ratio
196606	J82	Site 2: Yeo Creek fan	80	42	97 ± 9	4	162 ± 6	3	40.8 ± 2.4	26	3.81 ± 0.11	2.88 ± 0.09	25 ± 2	42 ± 2	**14.2 ± 1.0**	1.8 ± 0.2	3.0 ± 0.3
196602	J22	Site 1: Michael Creek fan	38	47	57 ± 10	6	389 ± 44	6	60.8 ± 2.7	22	3.38 ± 0.10	2.44 ± 0.08	17 ± 3	115 ± 14	**24.9 ± 1.5**	0.68 ± 0.13	4.6 ± 0.6
196603	J29	Site 1: Michael Creek fan	15	27	23 ± 4	4	155 ± 30	6	9.6 ± 0.8	21	4.42 ± 0.14	3.48 ± 0.12	5.3 ± 0.9	35 ± 7	**2.8 ± 0.3**	1.9 ± 0.4	12.7 ± 2.8
196604	J35	Site 1: Michael Creek fan	90	16	45 ± 7	5	297 ± 41	6	46.4 ± 2.5	19	3.97 ± 0.13	3.03 ± 0.12	11 ± 2	75 ± 11	**15.3 ± 1.1**	0.74 ± 0.13	4.9 ± 0.8
196605	J36	Site 1: Michael Creek fan	23	33	46 ± 6	10	294 ± 27	10	37.0 ± 2.7	24	4.16 ± 0.13	3.22 ± 0.11	11.1 ± 1.4	71 ± 7	**11.5 ± 1.0**	0.97 ± 0.15	6.1 ± 0.8
196607	J106	Site 1: Michael Creek fan	40	42	104 ± 8	4	150 ± 22	3	87.0 ± 6.3	21	4.06 ± 0.12	3.12 ± 0.11	26 ± 2	37 ± 6	**28 ± 2**	0.92 ± 0.11	1.3 ± 0.2
196608	J133	Site 1: Michael Creek fan	100	22	138 ± 8	4	253 ± 12	4	27.3 ± 1.2	29	4.45 ± 0.15	3.51 ± 0.13	31 ± 2	57 ± 3	**7.8 ± 0.5**	4.0 ± 0.4	7.3 ± 0.6
196609	J134B	Site 1: Michael Creek fan	40	55	467 ± 26	4	1268 ± 28	4	30.5 ± 1.5	27	2.83 ± 0.08	1.89 ± 0.06	165 ± 11	448 ± 19	**16.1 ± 1.0**	10.2 ± 0.9	27.8 ± 2.0
196610	J134C	Site 1: Michael Creek fan	50	24	152 ± 41	6	223 ± 36	4	28 ± 7	4	4.17 ± 0.14	3.23 ± 0.12	37 ± 10	53 ± 9	**9 ± 2**	4.2 ± 1.5	6.1 ± 1.8
196601	J6	Site 7: One Shot Hill	120	42	12 ± 3	5	83 ± 11	6	9.1 ± 0.3	22	3.88 ± 0.11	2.95 ± 0.10	3.1 ± 0.7	21 ± 3	**3.1 ± 0.2**	1.0 ± 0.2	6.9 ± 1.0
196611	J1258	Site 8: Styx River	2600	11	107 ± 71	2	189 ± 53	3	17.6 ± 1.6	23	3.81 ± 0.14	2.87 ± 0.13	28 ± 19	50 ± 14	**6.1 ± 0.6**	4.6 ± 3.1	8.1 ± 2.4
196612	1370A	Site 8: Styx River	50	25	67 ± 12	5	101 ± 11	4	13.0 ± 1.3	24	3.70 ± 0.12	2.77 ± 0.10	18 ± 3	27 ± 3	**4.7 ± 0.5**	3.8 ± 0.8	5.8 ± 0.9
196613	1370B	Site 8: Styx River	100	21	91 ± 22	6	205 ± 38	5	17.4 ± 1.3	23	3.67 ± 0.13	2.73 ± 0.11	25 ± 6	56 ± 11	**6.4 ± 0.5**	3.9 ± 1.0	8.8 ± 1.8

Note: w.c. - water content (%), (n) - number of aliquots.
Average dose recovery, IR_{50} 0.65 ± 0.02 ($n = 39$).
Average dose recovery pIRIR 1.26 ± 0.03 ($n = 39$).
Average dose recovery, quartz 0.8. ± 0.06 ($n = 36$).

deposited or reworked and quartz grains were bleached. Sample J133 (7.8 ± 0.5 ka) constrains the formation age of surface MC6 by representing when the surface was active, and the sediment was re-worked and re-bleached. J134C and J133 have IRSL/OSL age ratios (Table 1) indicating that they may have some or much inherited age, so on this basis 9 ± 2 ka is considered a maximum age for MC5 and all features that are geomorphically younger (R5/4, MC5t, R4/3). The minimum age for the suite of terraces is constrained by J29 which dates MC8. These three ages constrain the age of displaced features R4/5, MC5t, and R5/6 with a probability distribution defined by the probability distributions of the OSL samples in each Monte Carlo simulation. J134C (9 ± 2 ka) represents the maximum age for any of these features, as it is a maximum age for the sediment on the highest relevant surface, so it is used to define the maximum age for the features. J133 (7.8 ± 0.5 ka) is used as the

likely mean age for the features, and the mean of the feature age PDF is chosen from this sample's PDF. Although MC5 is geomorphically older than MC6, the possibility of some undefined amount of inherited age and the wide age ranges of the OSL samples on MC6 and MC4 means the age of MC5 is well represented by the bracketing samples. J29 is used to select the minimum age for the samples in each simulation. Using J29 as a minimum allows the slip-rate ranges to include the possibility that J134C and J133 have inherited age and the terrace sequence is actually younger. Because the three displacement measurements are slightly different but evaluated with the same age constraint, they produce a range of slip-rates that decrease with decreasing relative age. R4/5 has the fastest slip-rate at 1.7 (+1.1/−0.4) mm/yr, MC5t is 0.9 (+0.9/−0.4) mm/yr and R6/5 is 1.1 (+0.9/−0.5) mm/yr (Table 2). This is not indicative of a slip-rate that changes through time, rather an artifact of
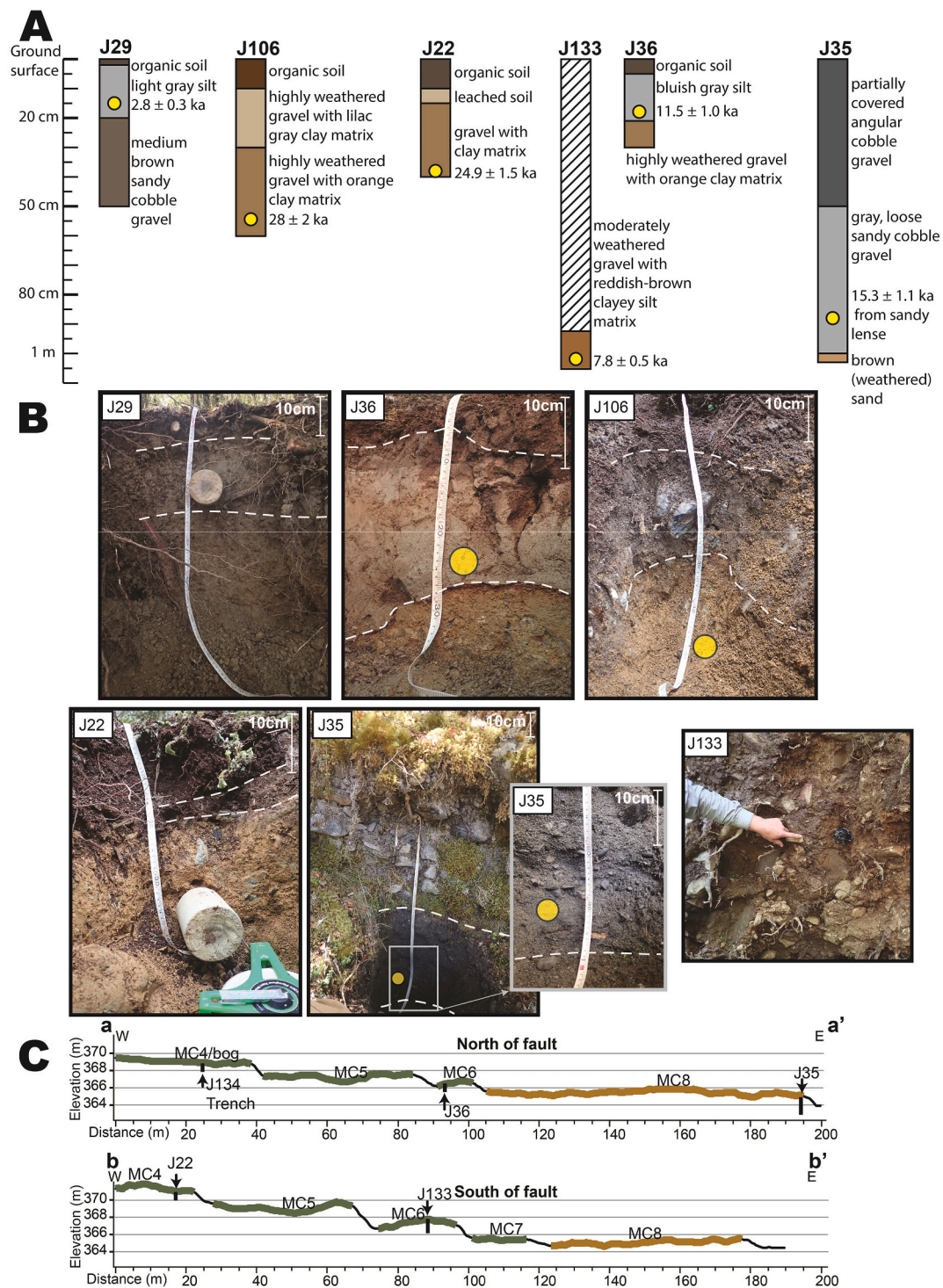
Fig. 5. A) Site 1: Michael Creek fan luminescence sample pit and outcrop stratigraphic logs showing the stratigraphy and depth of each sample. B) Photos of luminescence sample sites showing the sampled material and overlying sediment. C) Vertically exaggerated (~2× V.E.) annotated topographic profiles showing the elevation and sample locations for Site 1: Michael Creek fan. Profile locations are shown on Fig. 3A.

using the same age range (7.3 ± 1.4 ka) for three different features that likely have different ages that cannot be resolved with the current age control. We consider the R4/5 slip-rate of 1.7 (+1.1/−0.4) mm/yr to be the most robust, because if the OSL ages do have some inherited age, the slip-rate derived from the oldest displacement would be the least affected and closest to the true slip-rate.

4.2. Site 2: Yeo Creek fan

4.2.1. Geomorphic mapping

In the upper Taramakau River valley, a complex suite of alluvial fans in Yeo Creek and Joseph Creek are trimmed by the Taramakau River to form inset alluvial terrace surfaces (Figs. 2 and 7). The Hope Fault cuts these landforms with a single main trace and some discontinuous Riedel faults. The strike of the main trace changes from 85° between Yeo and
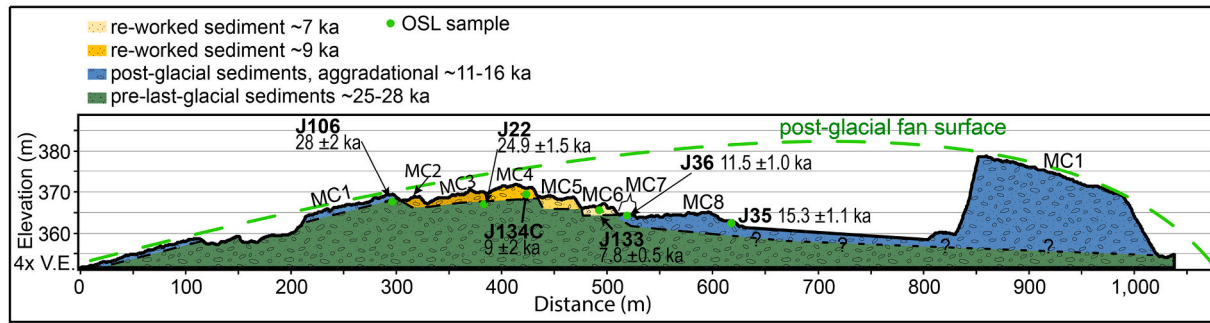
Fig. 6. Sediment schematic of Site 1: Michael Creek fan showing how the three generations of sediment (pre-last glacial, early post-last-glacial, and early Holocene) may be distributed. MCX labels refer to the named surfaces (Fig. 3). Post-glacial fan surface (lime green) corresponds to inferred post-glacial fan contours in Fig. 3. This schematic shows samples and stratigraphy primarily south of the fault on the upthrown side. It does not show the extended distribution of post-last glacial sediment onto surface MC4 north of the fault beneath the bog, samples J134B 16.1 ± 1.0 ka. (For interpretation of the references to colour in this figure legend, the reader is referred to the web version of this article.)

Table 2

Fault displacements and slip-Rates measured in this study. Included here are net-slip, strike-slip and dip-slip rates, and the feature age. The ranges shown here define the 95% CI of each probability distribution, and the preferred value defines the peak of the probability distribution. Surface/feature age min, max and preferred values are defined by a probability distribution describing the uncertainty of the OSL age, these distributions are defined in Appendix A. Slip-rate 95% CI has accounted for uncertainty from each of the inputs (surface/feature age, strike-slip displacement, vertical displacement, fault dip).

Site number and name	Displaced feature	Strike-slip displacement measurement (m)	Vertical displacement measurement (m)	Age of displaced feature (ka)	Net slip (mm/yr)	Strike-slip (mm/yr)	Dip-slip (mm/yr)
Site 1: Michael Creek fan	R4/5	9.4–12.1 (12.1 preferred)	2.0–2.3 (2.3 preferred)	7.3 ± 1.4	1.7 (+1.1/ −0.4)	1.6 (+0.9/ −0.6)	0.3 (+0.1/ −0)
Site 1: Michael Creek fan	MC5t	6.7 (+3.8/−3.6)	2.0 ± 0.1	7.3 ± 1.4	0.9 (+0.9/ −0.4)	0.9 (+0.9/ −0.5)	0.2 (+0.1/ −0)
Site 1: Michael Creek fan	R5/6	8.5 (+2.9/−3.3)	1.3–2 (1.3 preferred)	7.3 ± 1.4	1.1 (+0.9/ −0.5)	1.1 (+0.9/ −0.5)	0.1 (+0.1/ −0)
Site 2: Yeo Creek fan	JC R3/4	65 (+3/−5)	8.5 ± 0.5	11.7 ± 1.4	5.6 (+2.1/ −0.7)	5.6 (+1.7/ −1.1)	0.7 (+0.2/ −0.1)
Site 3: Locke Stream fan	KF1a (preferred reconstruction)	91 ± 13	6 ± 0.5	14.5 ± 1.6	6.2 (+2.7/ −1)	6.2 (+2.4/ −1.3)	0.4 (+0.1/ −0.1)
Site 3: Locke Stream fan	KF1b (alternate reconstruction)	51 ± 11	8.5 ± 0.5	14.5 ± 1.6	3.6 (+1.6/ −0.8)	3.6 (+1.5/ −1)	0.6 (+0.2/ −0.1)
Site 4: KF2	KF2	16 ± 6	21.4 (+6.5/−11.2)	13. ±2.9	2.0 (+2.5/ −0.7)	1.2 (+1.5/ −0.5)	1.6 (+1.9/ −1.0)
Site 5: KF3	KF3	80 (+18 /−17)	26.6 (+3.9/−3.3)	13. ±2.9	6.4 (+7.8/ −1.4)	6.1 (+6.9/ −2.0)	2.0 (+2.3/ −0.5)
Site 6a: Sackung Hill	SHa NNE fault	22 (+1/−5)	1.2 ± 0.2	16. ±0.5	1.3 (+0.1/ −0.4)	1.3 (+0.2/ −0.3)	0 (+0/−0)
Site 6b: Sackung Hill	SHb EW fault	22(+6/−3)	< 0.5	16. ±0.5	1.3 (+0.1/ −0.4)	1.3 (+0.2/ −0.3)	0 (+0/−0)
Site 8: Styx River fan	S1/S1b	–	21.5 ± 3.5	6.1 ± 0.5	–	–	6.3 (+3.2/ −1.9)

Joseph creeks to 70° west of Joseph Creek (Fig. 7). For the slip-rate calculations we assume the fault is vertical. The fault forms an uphill (north) facing scarp that is ~1 m high on the lowest terrace surface (YC2b), the scarp is higher on the older fan between Yeo and Joseph creeks where it juxtaposes younger incised surfaces (JC4 and JC5) with high remnant fan surfaces south of the fault (southern remnant). The interplay between Yeo Creek and Joseph Creek sourced sediment and lateral migration of the Taramakau River has created a series of trimmed alluvial fan surfaces (YC1 and JC1), advancement of younger fans (YC2, JC2 and JC3), and incision of Joseph Creek (details of geomorphic mapping and surface relative ages are presented in Appendix D). The Joseph Creek outlet into the Taramakau River is pinned by a high remnant of the JC3 fan south of the fault (southern remnant). As Joseph creek incised, the right lateral displacement of the fault facilitated preservation of a series of inset terraces east of the active stream channel (JC4, JC5). As displacement accumulated, it is possible that the east side of the channel on the south side of the fault (Fig. 7 marker vi) was eroded eastward, but there are insufficient landforms to determine with any confidence the extent to which this happened. The west edge of the southern remnant (Fig. 7, marker iv) correlates to the JC R3/4 that is

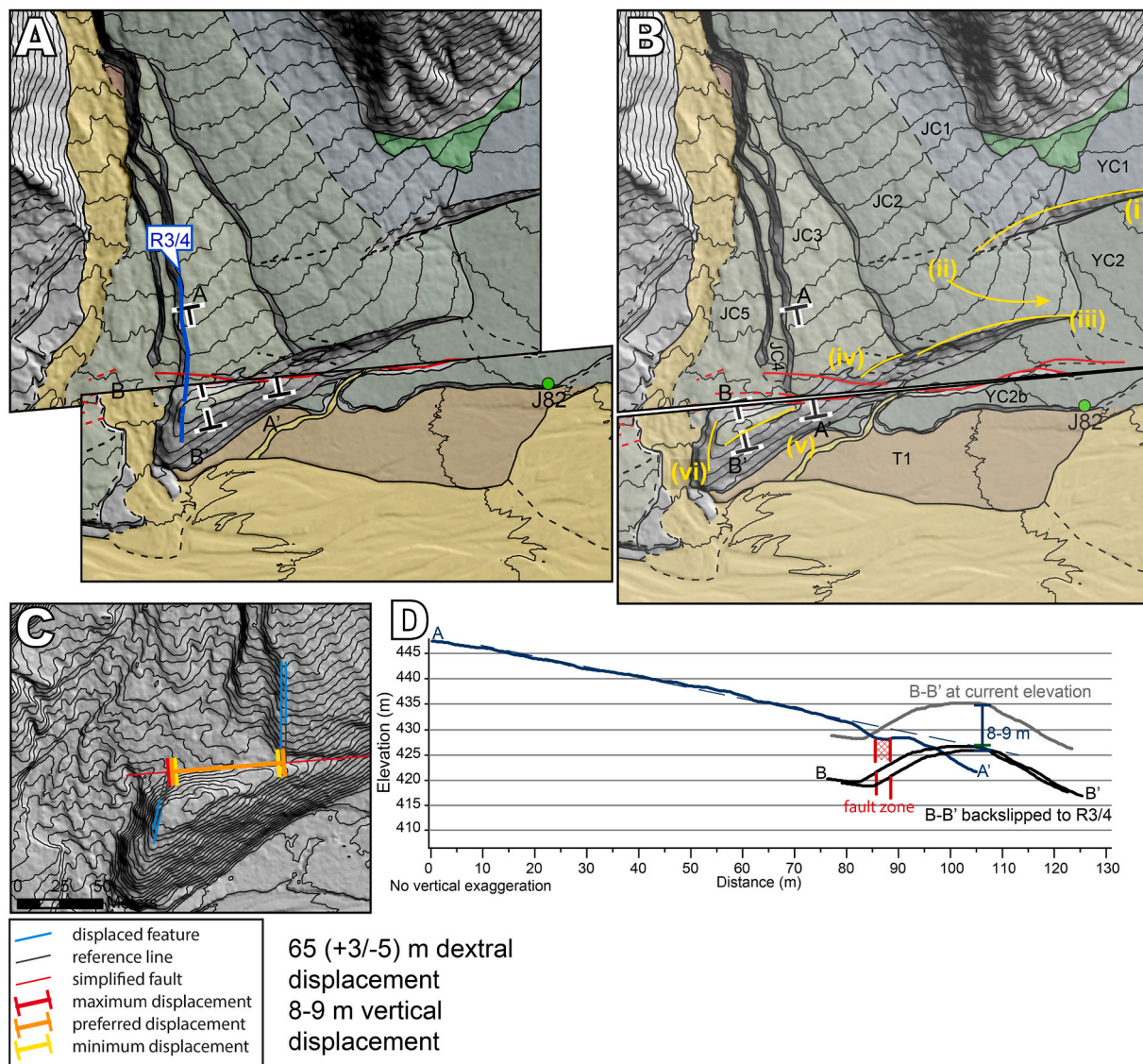used as the piercing point for the slip-rate measurement.

4.2.2. Displacement measurements

The west edge of the high fan remnant that forms the east bank of Joseph Creek south of the fault (southern remnant) can be matched to the riser between JC3 and JC4 (R3/4) north of the fault (Fig. 8A and B). The arcuate shape of the trimmed southern edge (Fig. 7, marker v) matches up with the toe of JC2 (Fig. 7 marker iii) if the fault is back-slipped so the west edge of the southern remnant (Fig. 7 marker vi) is aligned with the west edge of JC3 (R3/4). This implies that the remnant surface south of the fault corresponds with JC3 north of the fault. The remnant surface south of the fault is too small to confidently match the morphology to any surface north of the fault. If the fault is back-slipped to align the west edge of the southern remnant with the west edge of JC2 (R2/3), the arcuate cut of the toes does not line up, so we reject this backslip scenario. The maximum elevation of the remnant is higher than expected for a downslope projection of JC3 or JC2, indicating there has been some south side up displacement on the fault (Fig. 8D). Measuring the fault displacement from the western edge of the southern remnant (Fig. 7 marker vi) and the western edge of JC3 (R3/4), results in 65 (+3/

Fig. 7. Geomorphology of Site 2: Yeo Creek. A) Geomorphic map with geomorphic feature labels (black), markers of interest (yellow), and cross-section locations. White corner marks show the extent of Fig. 8. B) Topographic profiles of two major fan surfaces (solid line), location of the main trace of the Hope fault (red), and surface projection lines to the current local river level (dashed), maximum relative base level drop noted (maximum 40 m for a-a', maximum 15 m for b-b'). C) Schematic geologic cross-section (c-c') showing the early post-glacial fan sediments (blue), the re-worked but not reset sediments of the faulted YC2 terrace (green) from which sample J82 was collected, and the younger and surfaces of Yeo Creek and the Taramakau River (yellow). A stratigraphic log and photo of the outcrop where sample J82 was taken is in Appendix D. (For interpretation of the references to colour in this figure legend, the reader is referred to the web version of this article.)

−5) m displacement (Fig. 8C). This is a minimum displacement, because the western edge of the southern remnant (Fig. 7 marker iv) could be eroded eastward by the active stream.

4.2.3. Age constraints

At the Yeo Creek site, sample J82 was taken from sediments underlying the YC2b surface, accessed from the southern riser down to the T1 surface (Fig. 7). The OSL age of J82 is 14.2 ± 1.0 ka with IRSL/OSL ratios indicating possible incomplete bleaching (Table 1). Considering that this terrace is low in the valley and young relative to the local stratigraphy, we interpret the OSL age as being inherited from re-worked sediments of the higher/older fans and not representative of the formation age for T1. If there has not been any partial resetting of the luminescence age, then the J82 age of 14.2 ± 1.0 ka is a maximum age for YC2, YC1 and JC2, and all incised surfaces.

4.2.4. Slip-rate

The slip-rate was calculated using a triangular distribution for the displacement where the 5% and 95% confidence intervals are 60 m and 68 m respectively and the peak is at 65 m. For the age of this displacement, we use a PERT distribution where the minimum is 9 ± 2 ka based on the oldest incised post-glacial sediment at Site 1: Michael Creek. We chose this minimum age because before this time the valley went from

early postglacial sedimentation to stabilization and fluvial incision on the tributaries. For the maximum age, we use the sample J82 (14.2 ± 1 ka) because it represents the age of the early postglacial Yeo/Joseph Creek sediments and thus any incisional surfaces must be younger. We set the peak for the distribution using J36 (11.5 ± 1 ka) because it is the youngest un-reset post-glacial sediment in the valley, so around this time was likely when incision began. These constraints yield a slip-rate of 5.6 (+2.1/−0.7) mm/yr (Table 2). This slip-rate has two sources of significant uncertainty: there is no direct age control, and the displacement measurement is a minimum that may have post-displacement modification (eastward erosion of the west edge of the southern fan remnant). Both uncertainties leave room for the slip-rate to be greater than that presented here because the landforms may be younger than inferred or the displacement may be greater than measured.

4.3. Site 3: Locke stream fan

4.3.1. Mapping

On the east side of Locke Stream are two large alluvial fans (LS1 and LS2) and three alluvial terraces (LS3, LS4, LS5) (Fig. 9). The highest fan (LS1) surface is cut and displaced by the Kelly Fault, resulting in an uphill (south) facing scarp. The fault splays at the western side of the fan, producing a series of fault scarps which fan out to the NW and terminate

Fig. 8. Displacement measurement in the Yeo-Jacobs creeks area (Site 2). A) Back-slip reconstruction of the measured displacement. B) Original site map, showing the profile end points and location of sample J82. Yellow annotations show markers of interest, identical to those in Fig. 7. C) Detailed view of the displacement measurement, with 1 m contour interval. Minimum, maximum and preferred lateral displacements are shown. D) Topographic profile reconstruction. Profile A-A' shows morphology of the JC2 fan surface, with the dashed line showing the projected fan surface (now eroded). Red zones show the fault zone, which has been aligned on A-A' and B-B' to estimate the pre-faulting position of B-B′ relative to A-A'. The grey profile is B-B′ showing the southern fan remnant at its present elevation. The black profiles show B-B′ repositioned to match up with the projection of the JC3 surface, 8-9 m lower than the present elevation. (For interpretation of the references to colour in this figure legend, the reader is referred to the web version of this article.)

at the edge of the LS1 fan (Fig. 9 location i). The east edge of LS1 is delineated by a deeply incised, active stream channel which has a right bend where it crosses the fault (Fig. 9 location ii). The west and north-west side of the fan is defined by a riser which drops down to a lower fan (LS2) that emanates from Locke Stream and has a much lower slope than LS1. The LS2 fan is incised by the active Locke Stream, which has formed a series of terrace surfaces (LS3–5) at the distal end of the fan where the stream meets the Taramakau River. There is no surface morphology that is indicative of fault displacement or a scarp on LS2.

4.3.2. Displacement measurements

Displacements on the Kelly Fault at Locke Stream were estimated by correlating small channel and ridge features on the high fan surface (LS1) (Figs. 9 and 10). The channels and ridges formed while the fan surface was active and they were preserved when the fan surface was abandoned, then the measured offsets occurred after abandonment.

Lateral displacement measurements are made in map-view to account for various projection directions to the scarp for each feature. Two re-constructions of the LS1 surface are possible. The preferred reconstruction (KF1a) results in 91 ± 13 m dextral displacement and 6 ± 0.5 m vertical, south side up (Fig. 10). The second possible reconstruction (KF1b) results in 51 ± 11 m of dextral displacement and 8.5 ± 0.5 m vertical, south side up (see also Appendix D).

4.3.3. Age constraints

LS1 fan sediments (Fig. 9) are very poorly sorted with an abundance of large angular cobbles, so we did not attempt OSL sampling. The maximum age of LS1 is based on timing of glacial retreat determined in other nearby sites that opened the valley to sedimentation, and the timing of base level drop that initiated formation of the middle fan. Because LS1 is the oldest post-glacial deposit at the Locke Stream site, and slope instability is common during and after glacial retreat (e.g.,
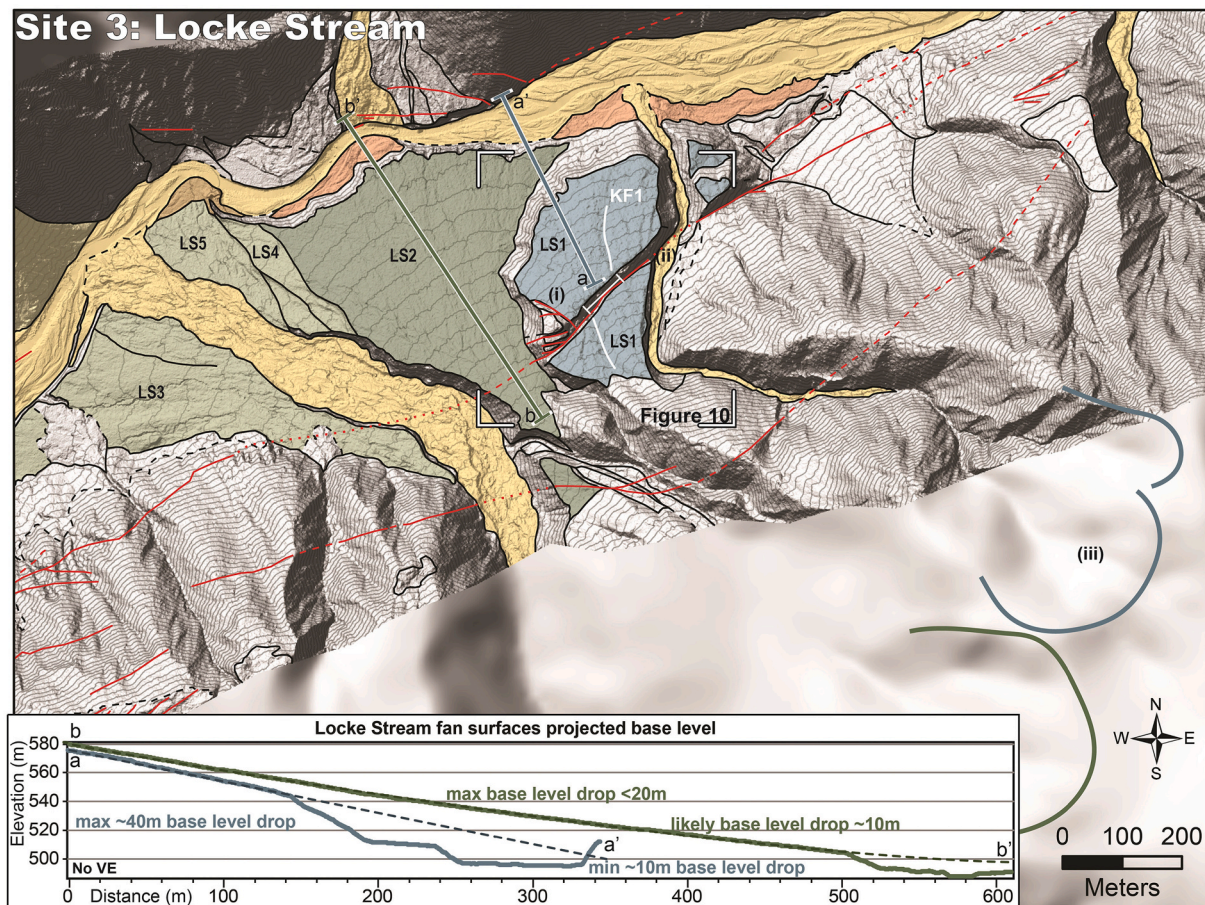
Fig. 9. Geomorphic map of Site 3: Locke Stream area. Displacement measurement KF1 is shown in black on the LS1 surface. Source area for LS1 is shown by (iii). Part of the source area for the LS2 fan is shown with green and includes the Locke Stream watershed. Profiles show maximum relative base level drop interpolated from the preserved fan slopes and limited by the valley width. Extent of Fig. 10 is indicated with the white corner marks. (For interpretation of the references to colour in this figure legend, the reader is referred to the web version of this article.)

Holm et al., 2004;Allen et al., 2011; Kos et al., 2016), we assume that LS1 is an early post-glacial feature. As discussed in Section 2, the age of the moraines on the coastal plain (Fig. 2 17.3 ± 0.5 ka, Barrows et al., 2013), indicates the valley was still occupied by ice at that time so LS1 must be older than that. OSL ages of alluvial sediments downstream in the Taramakau valley at Michael Creek provide intermediate ages for the ice retreat, when ice was gone from Michael Creek area but may have been still occupying the valley further upstream (oldest is J134B = 16.1 ± 1 ka, but this sediment might not be alluvial; the oldest clearly alluvial sediment sampled is J35 = 15.3 ± 1.1 ka). Ages of end moraines in Arthurs Pass (15.2 ± 0.8 ka, Eaves et al., 2017) indicate the time when ice was limited to the cirques and high elevations indicating the lower valleys (including the Locke Stream area) should have been completely free of ice. Thus, the maximum age limit for the fans at Locke Stream is 17.3 ± 0.5 ka, and the preferred age is 15.2 ± 0.8 ka.

The minimum age for the Locke Stream fans is more difficult to constrain. Downstream, the Yeo/Joseph creek and Michael Creek sites indicate that there has been 0 to 20 m of local base level drop since those fans formed, while LS2 at Locke Stream indicates 10 to 20 m of local base level drop has occurred since it was formed. This may indicate that LS2 is older than the fans downstream, or it may indicate a different local geomorphic environment where the confined Taramakau River has incised more deeply than the wide braided river downstream. At Michael Creek, incision of the early post-glacial fan was well underway at 9 ± 2 ka, so we use this for the minimum age of LS1.

4.3.4. Slip-rates

To derive slip-rates, we use the lateral and vertical displacements with the assumption of a steeply north dipping fault (80 ± 10°N). We set the maximum age for the fan as 17.3 ± 0.5 ka because at that time ice occupied the valley. The minimum age is set as 9 ± 2 ka, because by this time incision was underway at Michael Creek so the LS1 fan was likely also incised and abandoned. This yields a net slip-rate of 6.2 (+2.4/ −1.0) mm/yr for the preferred displacement of KF1 (Table 2). Due to the lack of direct dating and high uncertainty of the fan age, this slip-rate has a high uncertainty. The maximum age choice is quite conservative, but the fan could be younger than inferred, so 6.2 (+2.4/−1.0) mm/yr should be considered a minimum slip-rate for this site.

4.4. Site 4: KF2

4.4.1. Mapping

East of the Otehake River, the Kelly Fault cuts and displaces a hill spur (Fig. 11A location i). The fault trace cannot be precisely identified west of the spur where it crosses alluvial fans (Fig. 11A location ii). Some secondary faults of the Kelly Fault distributed deformation zone have been mapped on the hillside south of this fault trace (Fig. 11A location iii), but these faults do not cut and displace features that can be correlated across the fault trace.

4.4.2. Displacement measurement

To measure fault displacement here, we match the displaced ridge across one prominent trace of the Kelly Fault (Fig. 11B and C). The fault
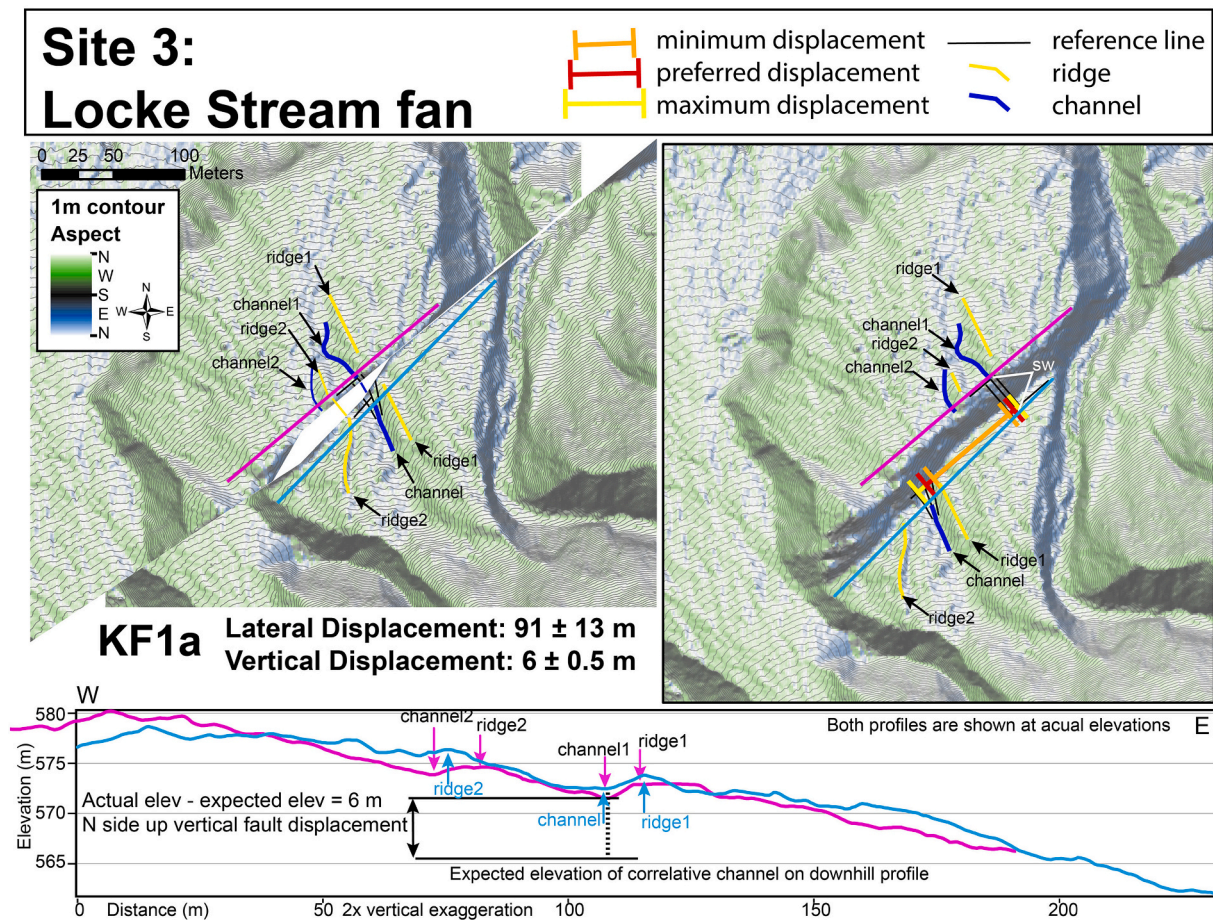
Fig. 10. Displacement measurement details for KF1 at Site 3: Locke Stream. A) Back-slipped map showing correlation of small ridge and channel features across the fault. B) Current site map with correlated features shown and minimum, preferred and maximum lateral displacement measurements. C) Fault parallel topographic profiles, laterally shifted to match the ridge and channel features and measure vertical displacement across the fault. Expected elevation difference is based on fan slope and scarp width (sw). Alternate reconstruction and displacement measurement, KF1b, is shown in Appendix D.

strike here is 070 ± 3°. The ridge is projected from the north side of the fault scarp to the fault trace at the base of the scarp. The maximum displacement assumes the ridge projects parallel to its trend across the scarp. The minimum reconstruction assumes there has been minimal erosion of the scarp and the ridge is projected across the scarp perpendicular to the fault. The strike-slip displacement is 16 ± 6 m (Fig. 11). The vertical fault displacement is measured by projection of fault perpendicular topographic profiles (Fig. 11D) to a vertical or north dipping fault plane, the vertical fault displacement is 21.4 (+6.5/−11.2) m, north side up.

4.4.3. Age control

There is no direct age control at this site. The maximum age of the ridge is no older than when ice occupied the valley. There is no constraint on the minimum age of the landforms. The age distribution used to calculate the slip-rate has an absolute maximum of 17.3 ± 0.5 ka, peak probability at ~15 ka, when the valley was definitely ice-free (based on age of end-moraines in Arthurs Pass, Eaves et al., 2017), and extends to present with low probability, so the absolute minimum age is 0 ka, but the 95% CI bounds are 6.5 ka and 17 ka. This age probability distribution is chosen under the assumption that the features are likely formed during the early postglacial landscape settling, but the total age range distribution includes the possibility that the landforms and displacement are significantly younger.

4.4.4. Slip-rate

Using the displacement and age as discussed, the net slip-rate is

estimated as 2.0 (+2.5/−0.7) mm/yr with a similar strike-slip and dip-slip-rates (Table 2). This slip-rate is produced by giving preference to an early postglacial age to the displaced ridge. However, ridges are an erosional feature and may be continually refreshed, so the feature and displacement may be on the younger side. The lack of direct dating of the displaced ridge means this slip-rate is uncertain, and the chosen age range means the slip-rate may be higher than indicated here. However, it is unlikely that the slip-rate is lower than this estimate because it is unlikely the ridge and accumulated displacement are older than the last glaciation.

4.5. Site 5: KF3

4.5.1. Mapping

West of Lake Kaurapataka, the Kelly Fault cuts a hill spur forming an uphill facing scarp (Fig. 11E). The slope has a channel remnant which trends perpendicular to the fault scarp and can be identified on both sides of the fault (Fig. 11F). This channel has similar cross-sectional morphology, longitudinal slope, and planform trend on both sides of the fault (Fig. 11G and H). On the south (uphill) side of the fault, the channel is obscured by deposition against the fault scarp (Fig. 11F). North of the fault, the channel does not reach to the top of the scarp, likely due to scarp degradation eroding the fault-proximal extent of the channel.

4.5.2. Displacement measurement

Fig. 11G shows the landscape around the displacement measurement
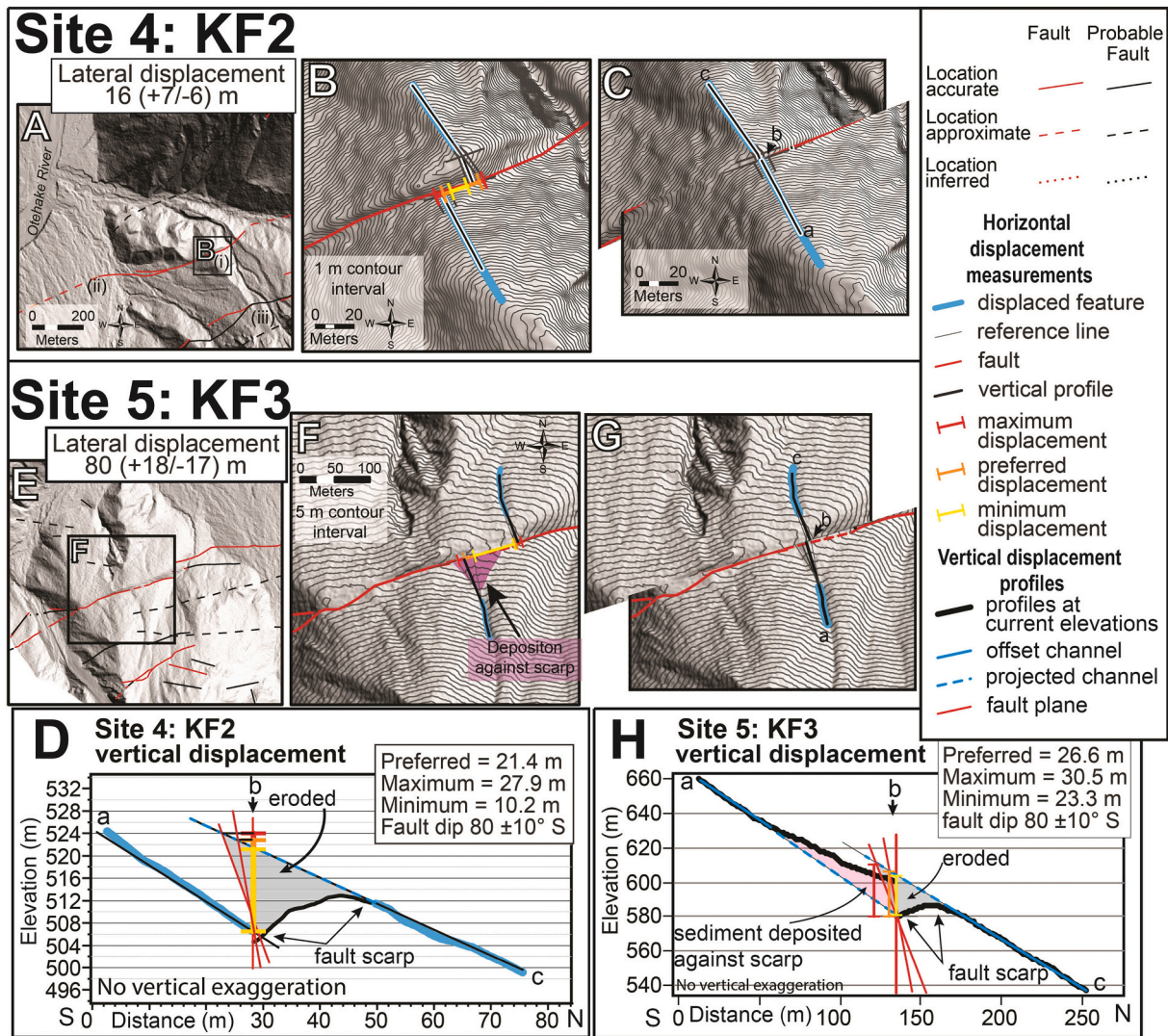
Fig. 11. Map and displacement measurement for Site 4: KF2 and Site 5: KF3. A) Site 4 Hillshade and fault map of area surrounding displacement measurement KF2. Roman numerals indicate locations mentioned in the text. B) Features and profiles at the displacement site. Lateral displacement measurements were made in map view as shown in this panel. The hanging wall (north) side of the ridge is projected to the simplified fault trace at the base of the scarp. C) Cut and back-slipped map of the displacement shows that the feature morphology matches across the fault. D) Fault perpendicular profiles along the ridge, shown at their current elevations. Letters a, b and c correspond to the letters in panel C. The hanging wall portion of the ridge (north of the fault) is projected to the fault plane, which is shown with a range of possible dips. The vertical distance between the fault trace on the footwall and the intersection of the projected hanging wall ridge and fault plane is the vertical fault displacement. E) Site 5, Hillshade and mapped faults of area surrounding displacement measurement KF3. F) Zoom of the displaced features at Site 5: KF3. Lateral displacement correlation shown with minimum, preferred, and maximum measurements. From the south, the channel is projected across the scarp along its trend. From the north the channel is projected to the scarp through the accumulated sediment along a range of trends similar to the trend south (uphill) of the sediment. G) Cut and back-slipped map of the displaced features at KF3. This view shows how the channel and the subtle features nearby correlate well when the landscape is restored to the preferred fault displacement. H) Fault perpendicular profiles along the KF3 displaced channel; a, b and c correspond to the letters in panel C. On the south side, the channel is projected to the fault scarp beneath the accumulated fan sediments. On the south side, the channel is projected across the scarp to the estimated fault plane. The height from the level of the fault trace at the base of the scarp to the intersection of the projected channel and the fault plane is the vertical fault displacement. Unannotated hillshade and contour maps of sites 4 and 5 are in Appendix D.

laterally restored. Not only does the identified channel correlate across the fault, more subtle features just west of the channel also correlate with the same amount of fault displacement. The lateral displacement of the channel is 80 m (+18 m/−17 m), with most of the uncertainty being from the projection of the channel to the fault scarp. Since both channel remnants have the same trend and slope and are fairly straight, we prefer the straight projection of the southern channel remnant to the fault. We measured the lateral displacement parallel to the apparent strike of the fault.

The vertical fault displacement is estimated using fault perpendicular topographic profiles (Fig. 11H). Profiles along the channel segments north and south of the fault to the fault trace show that the channels

have similar slope, where they are not covered (south of the fault) or eroded (north of the fault). The un-modified sections of each channel segment is projected across the fault in profile view. The footwall (north) side is projected to the mapped fault trace at the base of the fault scarp. The hanging wall side (south) is projected beyond the fault scarp to the fault planes that are drawn extending up from the fault trace. The vertical displacement is the height between the fault trace at the base of the scarp and the intersection of the projected fault plane and the projected channel. A range of fault dips are used, vertical to 70°N, resulting in a range of vertical displacement measurements. Vertical fault displacement is 26.6 (+3.9/−3.3) m (Fig. 11H).

4.5.3. Age control

There is no direct age control at this site. The maximum age of the channel is no older than when ice occupied the valley. We have no constraint on the minimum age of the landforms. The age distribution used to calculate the slip-rate has an absolute maximum of 17.3 ± 0.5 ka, peak probability at ~15 ka, when the valley was definitely deglaciated, and extends to present with low probability, so the absolute minimum age is 0 ka. We chose the peak probability as 15 ka under the assumption that the features are likely formed during the early postglacial landscape settling.

4.5.4. Slip-rate

From the displacement measurement and age assumptions the net slip-rate for the Kelly Fault at KF3 is 6.4 (+7.8/−1.4) mm/yr (Table 2). The lack of age control means this slip-rate has high uncertainty, but the landforms and displacement are unlikely to be older than the inferred maximum age of 17.3 ka, so the slip-rate is unlikely any slower than the minimum presented here (5.0 mm/yr).

4.6. Site 6: Sackung hill

Vermeer et al. (2021) presented an overview of the structure and geometry of Sackung Hill and identified two sets of tectonic faults among the gravitational fault network (Fig. 12). These faults are postulated to transfer tectonic slip from the Hope Fault near Michael Creek to the Kelly Fault south of Sackung Hill. Alternatively, the Sackung Hill tectonic faults may be part of a distributed deformation zone between the Hope and Kelly faults. The significance of each interpretation is presented in the discussion section. One site on each tectonic fault set is selected to determine a minimum tectonic slip-rate based on displacement of glacial striations (Fig. 12).

4.6.1. Age control

The glacial striations on Sackung Hill formed when there was ice filling the valley and ceased to be modified once the ice stagnated. We have made the assumption that these are not relict striation from previous glaciations. Moraines at Lake Brunner indicate the whole valley
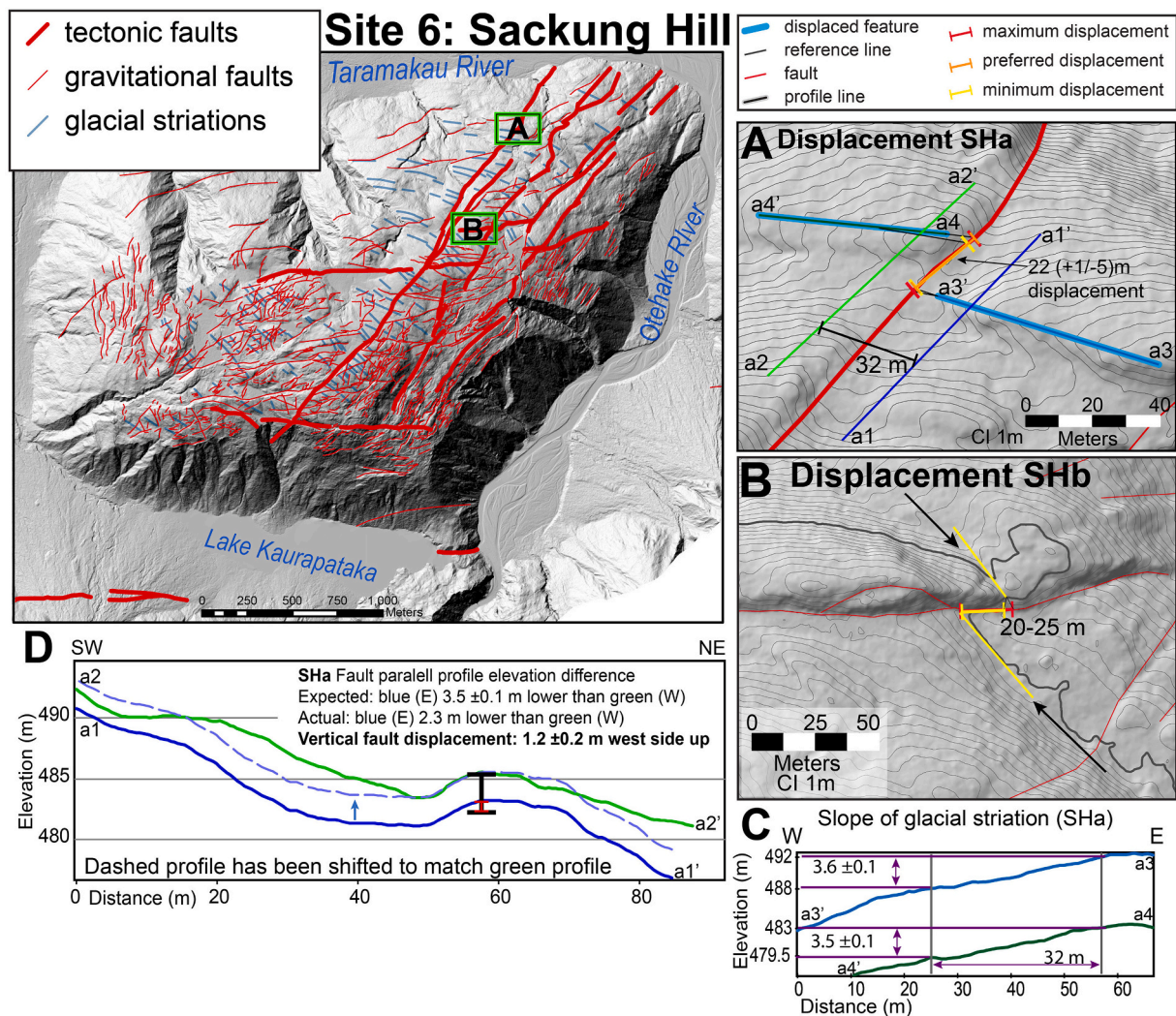
Fig. 12. Map of Site 6: Sackung Hill, with fault mapping from Vermeer et al. (2021), locations of displacement measurement maps are shown in green. A) Details of displacement site Sha on the NNE striking fault. The profile lines in panel C and D are shown, the lateral displacement measurement, and the separation between the fault parallel profiles. B) yellow line shows the slope change feature used to measure the offset. The highlighted contour shows that the feature is nearly horizontal on the south side and is at the same elevation on the north side, indicating no vertical displacement. Minimum and maximum lateral displacement measurement is also shown. C) Profiles a3 and a4 are shown here, and the purple lines show how the expected elevation difference (a3-a3', 3.5 ± 0.1 and a4-a4', 3.6 ± 0.1) based on the feature slope was estimated. D) Fault parallel profiles used to calculate vertical fault displacement. The solid profiles are at their real, current elevation and the dashed blue profile (a1-a1') has been shifted up to match the green (a2-a2'). The expected profile elevation difference is 3.5 ± 0.1 m, based on the striation parallel profiles. The actual elevation difference is 2.3 m, so the vertical fault displacement is 1.2 ± 0.2 m west side up. (For interpretation of the references to colour in this figure legend, the reader is referred to the web version of this article.)

was under ice at 17.3 ± 0.5 ka when they were formed(Barrell et al., 2011; Barrows et al., 2013). At 15.2 ± 0.8 ka the end moraines at Arthurs Pass formed (Eaves et al., 2017), indicating that the ice had retreated from the valleys by this time. Thus, the striations were formed between ~17 ka and ~ 15 ka. This glacial retreat age is supported by the OSL ages from fluvial or alluvial deposits upstream, which indicate that by 14–15 ka the upper Taramakau valley was free of ice. Based on these constraints on the timing of glacial retreat, we set the age of the glacial striations as 16 ± 1 ka with a normal distribution.

4.6.2. Site 6a: Displacement SHa

This glacial striation is low on the NE corner of Sackung Hill (Fig. 12). It is cut by a NNE striking, steeply west dipping fault interpreted by Vermeer et al. (2021) as a tectonic fault. We use the crest of the striation as a linear piercing point to measure lateral and vertical displacement (Fig. 12A). We measure 22 (+1/−5) m of lateral displacement. Fault-parallel profiles are used to match the striations, and fault-perpendicular profiles to determine the expected vertical offset of the fault parallel profiles before faulting based on the striation slope (Fig. 12 profiles). The difference between the actual (current) elevation difference of the two fault-parallel profiles, and the expected difference based on striation slope, is the fault displacement 1.2 ± 0.2 m west side up (Fig. 12D). Based on the slight concave to the NW fault trace shape, the dip of this fault is 80 ± 10°NW. The net slip-rate is 1.3 (+0.1/−0.4)

mm/yr, with primarily dextral displacement (Table 2).

4.6.3. Site 6b: Displacement SHb

This displacement site is located on an E-W striking sub-vertical fault between two NNE-striking faults. The identified striation and trough match across the fault, and the slope change shown by the yellow line in Fig. 12B is used as the piercing line. The feature is at about the same elevation on both sides of the fault, the height of the scarp is produced by laterally displaced topography. The feature has little longitudinal slope and it reaches to the fault scarp, so there is no need to account for the longitudinal slope of the feature in measuring the vertical displacement. We measured 22 (+6/−3) m of dextral displacement and < 0.5 m of vertical displacement. This yields a net slip-rate of 1.3 (+0.1/−0.4) mm/yr (Table 2), assuming a vertical fault plane.

4.6.4. Discussion of Sackung hill slip-rates

These measured displacements show offsets that exceed plausible single event displacements for tectonic faults, indicating these faults have been active in multiple earthquakes. These sites and others on Sackung Hill have depocenters against the faults, giving them potential for yielding earthquake timing via paleoseismic investigations. Future investigations should be aware of possible gravitational fault slip that may not be triggered by tectonic slip (earthquake) on associated and nearby tectonic faults (see Appendix D for nearby evidence of late
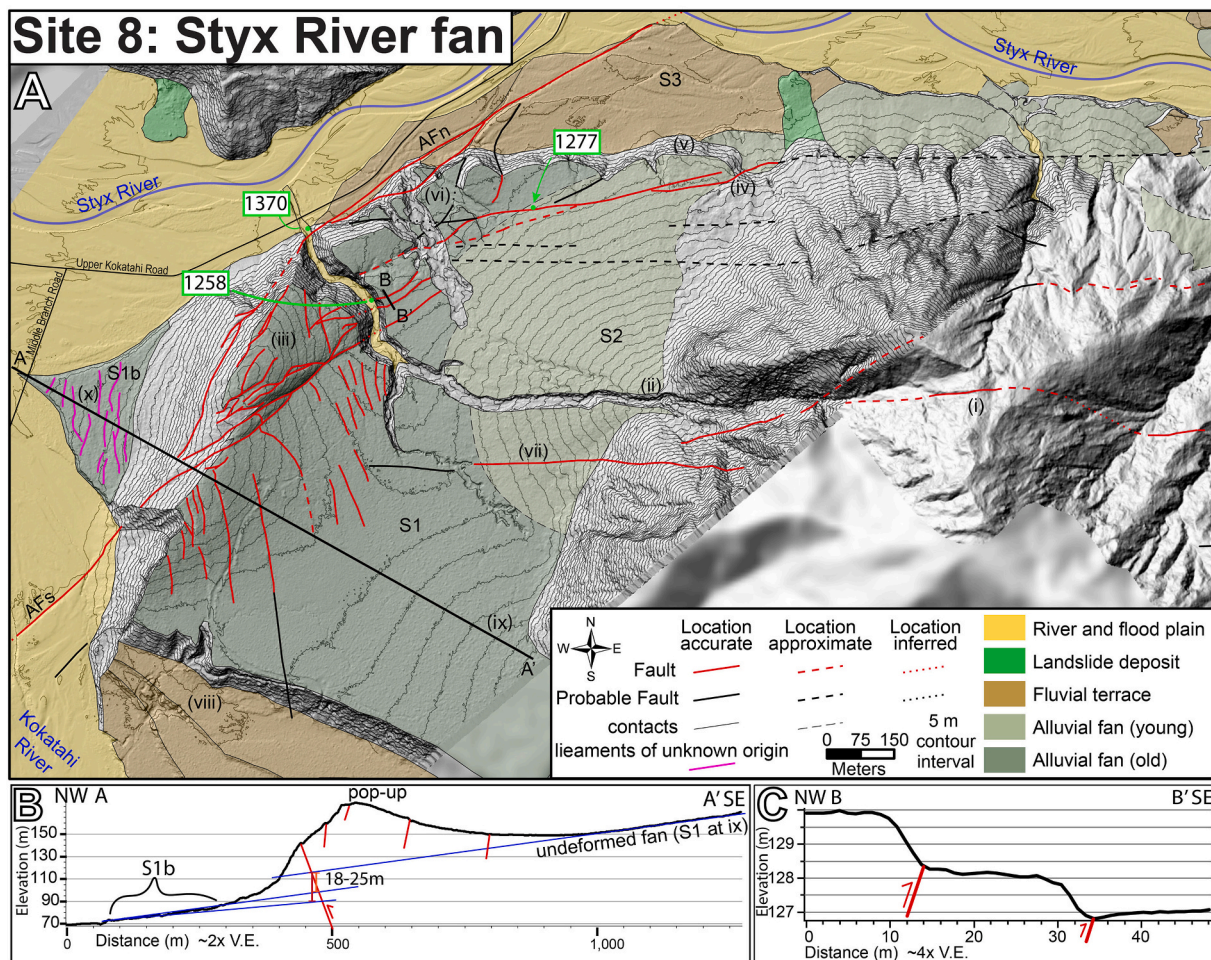
Fig. 13. A) Geomorphic map of Site 8: Styx River, with trench and exposure sites and topographic profiles. Location of interest referenced in the text are indicated with lowercase roman numerals in parentheses. The locations of trenches and outcrops are shown in green boxes. Fault mapping is from Vermeer et al. (2021). Geomorphic unit mapping has been refined for this study. B) Topographic profile used for vertical slip-rate measurement. Blue lines are the projections of S1 and S1b to the inferred fault plane, which is shown in red. Vertical displacement is 18–15 m. C) Topographic profile of fault scarp of the fault exposed at site 1258. (For interpretation of the references to colour in this figure legend, the reader is referred to the web version of this article.)

Holocene to historic gravitational fault displacement at Site 7: One Shot Hill) The slip-rates we have measured on Sackung Hill are minimum constraints for the total tectonic slip being accommodated by this fault network, because there are multiple faults in the network with similar structural significance on which we could not make a precise displacement measurement.
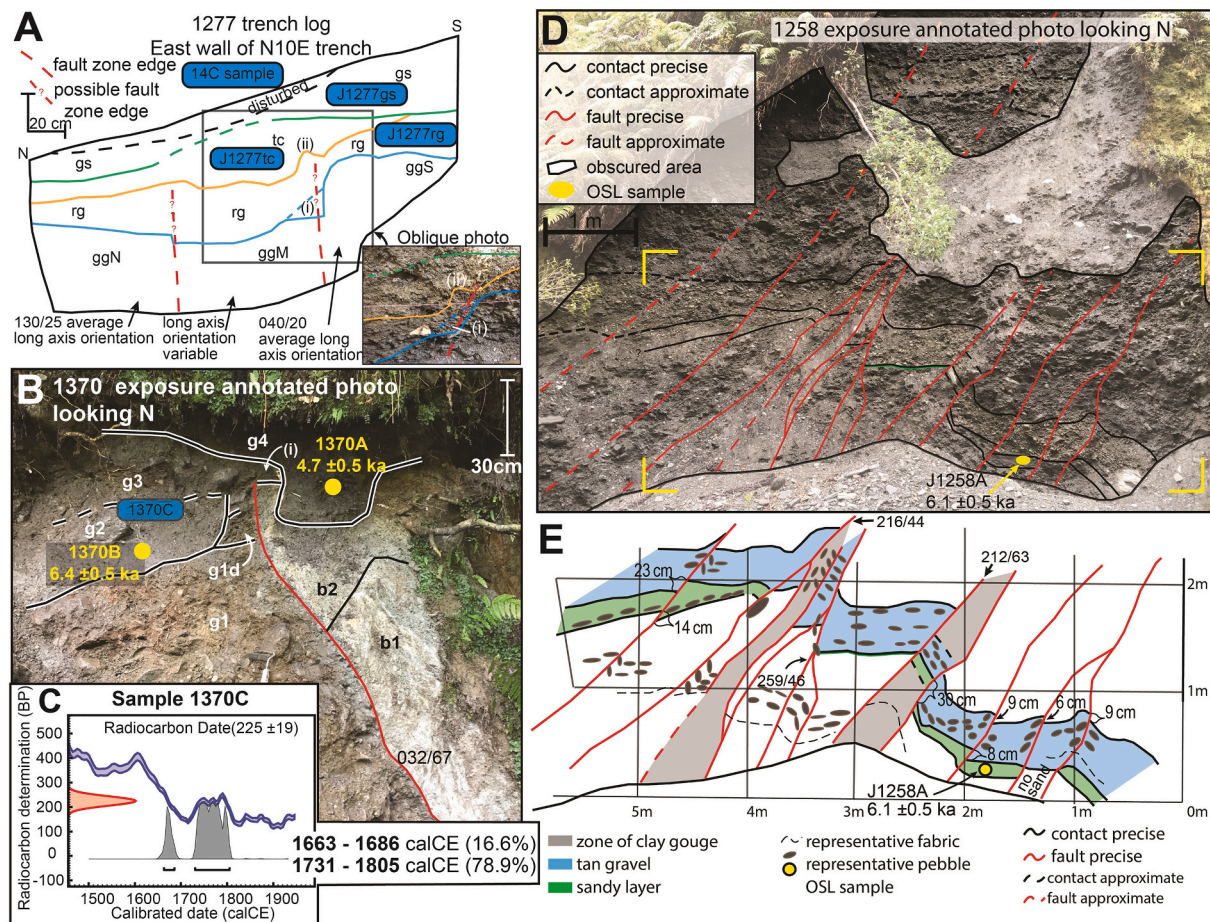
4.7. Site 8: Styx river

4.7.1. Mapping

The Styx site is located between the Styx and Kokatahi rivers where they converge and at the base of the range front along the Alpine Fault (Fig. 2, site 8). The range front has a small saddle (Fig. 13, location i) south of the Styx River which has been previously mapped as the location of a splay of the Kelly Fault (Langridge et al., 2016). Between the two rivers there is a large smooth arcuate alluvial fan (Fig. 13, surface S1). In the center of the fan, a secondary overtopping fan surface emanates from the rangefront saddle (Fig. 13, surface S2). The stream

(Fig. 13, location ii) which deposited this top fan flows west and has incised deeply to meet the Styx River. The western edge of S1 is uplifted and deformed by the Alpine Fault (Fig. 13, AFs and AFn), which has a ~ 300 m wide left step as inferred from the fault trace normal distance between adjacent strands of the Alpine Fault (AFn and AFs). The left step has formed a pop-up structure (Fig. 13, location iii), which deforms the western portion of the smooth S1 fan surface. West of the Alpine Fault, a fan surface remnant (Fig. 13, surface S1b, location x), which is covered with ~N trending lineaments of unknown origin, may be correlative to the S1 surface east of the fault.

East of the Alpine Fault, on the north side of the S1 and S2 surfaces, a splay of the Kelly Fault strikes ~E-W and creates a 2–3 m high north facing scarp (Fig. 13, location iv). North of this Kelly Fault scarp, a river cut forms the ~35 m high riser (Fig. 13, location v) between the upper fan surface and a low relief fluvial terrace of the Styx River (Fig. 13, surface S3). Where the Kelly Fault splay meets the pop-up (Fig. 13, location vi) the interacting faults form a series of steps that are likely fault scarps but also modified by low flow stream channels. There is a

Fig. 14. Observations and samples from exposures at Site 8: Styx River fan. A) Log of the east wall of the hand-dug trench 1277 with annotated photo. Photo was taken oblique to the trench wall, extent indicated on log with black box. 14C sample locations are shown in blue, parenthetical roman numerals reference positions mentioned in the text. Colours of unit contacts correspond to annotations in the photo. The central area between the dashed red lines of non-imbricated gravel is interpreted as the fault zone. Section of disorganized gravel (ggM) is interpreted as a fault zone, on either end of the trench exposure the gravel is well imbricated. It is uncertain if unit rg is faulted or simply deposited over the rough surface topography of gg, but the rough upper contact of rg suggests the unit is faulted. Upper units tc and gs are not interpreted as faulted. All three 14C samples returned modern ages. B) Exposure 1370 at Site 8, photo with annotations and sample locations. A) Solid lines are sharp contacts, dashed lines are gradational contacts. Fault is shown in red, fault strikes 032° and dips 67°E. OSL samples are shown with yellow circles, 14C sample location with blue oval. Sheared bedrock units (b1 and b2) in the hanging wall of the fault. Deformed gravel units (g1 and g2) are in the footwall and undeformed gravel (g3) and sand (g4) overlie the fault and unit b2. Units are further described in the text. B) Calibration curve for 14C sample 1370C, calibrated age is 1663–1805 CE (OxCal v4.4.4 Bronk Ramsey, 2009; Atmospheric data from Hogg et al., 2020). C and D) Exposure 1258 at Site 8, annotated photo and gridded outcrop log. The yellow circle indicates the location of OSL sample 1258A. Distinctive tan gravel unit and underlying thin sand are shown in the annotated log. Numbers in the annotated log indicate either apparent vertical displacement of a marker bed (cm), or the strike/dip of a fault. (For interpretation of the references to colour in this figure legend, the reader is referred to the web version of this article.)

second E-W striking splay of the Kelly Fault crossing S2 expressed as a very small scarp (Fig. 13, location vii). The south side of S1 is incised by a series of three fluvial terraces formed by the Kokatahi River which step down to the current river level (Fig. 13, location viii).

In three locations we documented faulting of this fan and took OSL and radiocarbon age control samples. These sites are individually described below.

4.7.2. 1277 Trench

Trench 1277 is located on the northern splay of the Kelly Fault near the toe of fan S2 at the base of the 2–3 m high scarp. The trench is 2 m long and 1.5 m deep and trends 010°, roughly perpendicular to the fault trace (Figs. 14 and 13A). The trench exposes a sequence of imbricated, lenticular schist-source cobble gravel (unit gg, Fig. 13A) covered with a series of finer grained sediments (units rg and gs, Fig. 13A) including a likely colluvial deposit (unit tc, Fig. 13A). The central section of unit gg has disrupted imbrication, with little to no grain orientation preserved, which we interpret as a zone of faulting (see Appendix D for more details of the trench log).

The disruption of gravel imbrication and the step in the upper contact of gg are interpreted to indicate faulting. Unit rg may be faulted, indicated by the irregular upper contact, but the lack of clear internal deformation of this sediment package leaves some uncertainty around whether it is faulted or just deposited over the scarp. Because this trench is small relative to the size of the scarp, it is likely only exposing a small section of the fault zone. All radiocarbon samples collected from this trench yielded modern ages (Fig. 14A). Because there has been no historic surface rupture on this fault or nearby faults the modern C14 samples provide no paleoseismic information. If unit rg is faulted, the material sampled for C14 from that unit (J1277rg) are likely ingrown rootlets rather than detrital twigs; the modern C14 age from unit rg does not preclude it from being interpreted as faulted.

4.7.3. 1370 Exposure

The 1370 exposure is a natural outcrop located in the north bank of the large creek where it has incised through the Alpine Fault pop-up (Fig. 14 and Fig. 13 B). The outcrop exposes highly sheared bedrock (units b1 and b2, Fig. 14B) in the hanging wall and unconsolidated gravel and silt deposits (units g1 and g2, Fig. 14B) in the footwall of a fault striking 032° and dipping 67° SE; the stratigraphy is described in detail in Appendix D. We sampled the faulted silt deposit (g2, Fig. 13B) for OSL (sample 1370B, Table 1, 6.4 ± 0.5 ka) and C14 (sample 1370C 1633–1805 CE, Fig. 13C). A sand deposit (unit g4, Fig. 13B) overlies all the other units and appears undeformed above the fault; we sampled this unit for OSL (sample 1370A, Table 1, 4.7 ± 0.5 ka).

The order of magnitude age discrepancy between the C14 and OSL ages may be explained in two ways that are not mutually exclusive. First, the material C14 dated may be infiltrated rootlets that do not represent the depositional age of the sediment; if this is the case, the C14 age is a minimum sediment deposition age because the sediment had to be in place before roots could grow into it. Alternatively, the C14 dated material could have been incorporated into the sediment during deposition and may be older than the deposition or representative of the depositional age. Second, the OSL may or may not have been bleached and reset at the last deposition. Unfortunately, the IR/OSL age ratios do not make it clear that the quartz luminescence signal was reset, but also they do not rule out bleaching and resetting, we simply cannot know for sure. However, if the quartz was bleached so the OSL age was reset when these sediments were deposited here and 6.4 ± 0.5 ka and 4.7 ± 0.5 ka are accurate depositional ages, this would imply that this specific splay of the Alpine Fault has not had surface rupture in the last ~4 kyr because unit g4 is not faulted. Considering the position of this fault splay along the active trace of the Alpine Fault, we consider it unlikely that it has not had surface rupture in ~4 kyr, and prefer the interpretation that the OSL ages were not fully bleached during transport and deposition in the present location. Thus, we consider the C14 age of 1633–1805 CE to be

more closely representative of the depositional age of unit g2. Unfortunately, the uncertainty around the source of the C14 material (depositional detritus or in-grown rootlets) means we cannot apply this age as either a minimum or maximum bound for the one or more surface ruptures which have deformed unit g2.

4.7.4. 1258 Exposure

This exposure is in the main creek about 200 m upstream of the road on the north side of the stream (Figs. 13 and 14C). The stream is deeply incised into the fan with steep walls ~30 m high. The base of a small slip exposes in-situ sandy gravel low in the fan stratigraphy (Fig. 14C). The sediments are faulted by multiple NNE-striking, west dipping faults. Within the faults, the sub-rounded to well-rounded, lenticular clasts are rotated from their imbricated depositional position to vertical or completely disorganized, and the matrix contains more clay. Measured in the outcrop, the faults strike 212–216° and dip 40–60° NW. The discontinuity and variable thickness of the marker units suggests there is strike-slip displacement perpendicular to the plane of the outcrop that juxtaposes lateral variations in the bed thickness. Apparent reverse displacement of sandy and tan marker beds suggest that these faults may have some component of reverse slip, though depending on bedding orientation and thickness variations, strike-slip displacement could produce these apparent reverse displacements. Total apparent vertical displacement across the outcrop is 2 ± 0.1 m measured on the base of the tan gravel (Fig. 14C). The fault projects up to a scarp on the S1 fan surface along the east edge of the pop-up structure with vertical displacement of 1.8 ± 0.2 m (Fig. 13), indicating that most or all of the apparent dip-slip displacement on this particular splay occurred after the fan sediment had accumulated and the surface became geomorphically inactive. The amount of lateral sip on this particular fault splay is undefined; there are no suitable geomorphic markers on S1. The OSL sample of a sandy lens at the base of the exposure yielded 6.1 ± 0.5 ka, with IR/OSL ratios indicating potentially poor bleaching (Fig. 14C, Table 1). However, mid-Holocene is a reasonable age for the S1 fan formation so we consider this OSL age as a maximum age for the S1 surface. Previous mapping has estimated the age of this fan surface as Late Pleistocene (Nathan et al., 2002) or Holocene (Barrell et al., 2011).

4.7.5. Slip-rate

These three exposures and the morphologic mapping are consistent with the interpretation that S1 is a mid-Holocene alluvial deposit that has been uplifted by the hanging wall of the Alpine Fault (Fig. 13A). Faulting is documented on morphologic scarps on both the east (exposure 1370, Fig. 14B) and west (exposure 1258, Fig. 14C) sides of the pop-up on faults parallel to the Alpine Fault, and also on an east-west striking splay of the Kelly Fault east of the pop-up (trench 1277, Fig. 14A). The OSL sediment ages indicate that the fan sediment is 6.1 ± 0.5 ka (sample J1258), so this fan is mid-Holocene in age. We were unable to identify any laterally displaced features that could be correlated across the faults with an absolute age to get a lateral slip-rate measurement. The eastern side of the S1 fan surface appears undeformed but is uplifted in the hanging wall of the Alpine Fault. The surface remnant west of the Alpine Fault (S1b) may correlate with S1 east of the fault, allowing measurement of a vertical slip-rate. We do not have observations on the stratigraphy or age of the western surface remnant, only the surface morphology, so the correlation of these surfaces is tentative. It is possible that S1b is younger than S1, or that S1b has been eroded and the surface correlative to S1 would have been at a higher elevation. Assuming S1 and S1b are correlative, projection of both surfaces to the main trace of the Alpine Fault yields 21.5 ± 3.5 m of vertical displacement (Fig. 13B). This measurement disregards the vertical displacement within the pop-up, because this structure is formed primarily by the lateral slip on the fault and is not representative of the vertical or dip-slip-rate below the surface complexities. The resulting dip-slip-rate of the Alpine Fault, using J1258A as the maximum age, is 6.3 (+3.2/−1.9) mm/yr dip-slip assuming a 50 ± 10° E fault dip (Table 2).

4.7.6. Earthquake timing

The radiocarbon sample J1370C (1663–1805 CE, Fig. 13B) was taken from sediments faulted by at least one surface rupture on the Alpine Fault main trace. If the dated twigs are actually rootlets, their age is younger than the sediment deposition. However, if they are detrital twigs, the sample age represents the depositional age of the sediment and is a maximum age for at least one surface rupture. The sample has a large calibrated age range (Fig. 13C), and we lack additional stratigraphically related samples that can be used for OxCal modelling to constrain the depositional age more precisely. The age range is such that the post-depositional surface rupture could have been the 1717 Alpine Fault earthquake, or the more recent early 1800's Alpine Fault earthquake identified 3 km to the south (Fig. 1, site B; Langridge et al., 2020) and in Lake Kaniere (Fig. 1, Site A; Howarth et al., 2021).

4.8. Other sites

Two other sites were investigated in detail and are discussed in Appendix D; Site 7: One Shot Hill and Site 9a: Lake Kaurapataka tree. At Site 7, evidence for Late Holocene gravitational slumping was found in deformed alluvial fans. At Site 9a, evidence for a ca. 1753–1848 death age of a drowned tree is tentatively attributed to strong proximate ground shaking. The source of the shaking is not known but the Hope-Kelly-Alpine Fault system is considered a likely source.

5. Results: Coulomb stress transfer modelling

5.1.1. Modelled earthquake scenarios

We modelled six earthquake scenarios using the parameters shown in Table 3. Source ruptures are terminated at points where the earthquake meets a structural complexity such as a branching node on a major fault. The models present plausible rupture scenarios based on geological data (e.g., Rodgers and Little, 2006). All the source earthquakes modelled are finite fault slip solutions rather than reflecting the progressive dynamic rupture of an earthquake. A propagation direction can be incorporated into the interpretation by using the resulting CFS at a fault intersection to evaluate which splay might be preferred for continued rupture (Parsons et al., 2012), but the models themselves have no assigned propagation direction.

In the simulated source ruptures, displacement is scaled with rupture length and Mw and slip distributions progressively reduce to zero at the rupture end points. The proportion of slip at the surface relative to slip at depth was chosen based on Dolan and Haravitch (2014), based on estimated cumulative slip of each fault (central Hope Fault up to 13 km, Langridge et al., 2014; Kelly Fault <2 km, Nathan et al., 2002). The full Kelly Fault southern splay rupture has a high maximum displacement in order to reach the desired magnitude (derived from surface trace length) on the westward, vertically decreasing fault area where the fault intersects the Alpine Fault. The modelled Alpine Fault rupture through the intersection zone has a homogenous slip distribution so specific earthquake parameters would not affect the resulting pattern of CFS.

5.1.2. Alpine Fault earthquakes

Model 1 (Fig. 15 A1) simulates an earthquake on the central Alpine Fault with the north end of the rupture at the surface intersection of the southern splay of the Kelly Fault and the Alpine Fault (essentially stopping just south of the Styx site, Fig. 15 A1). This earthquake positively stresses the Alpine Fault north of the rupture termination, and the entire Hope-Kelly Fault system. The magnitude of positive stress broadly decreases with distance from the rupture termination, but also displays variation among fault planes at similar distances due to variations in fault geometry. For example, the Kelly Fault splay tips receive higher positive stress change than the immediately adjacent Alpine Fault plane (Fig. 15 A2). The magnitude of positive stress on the southernmost splay of the Kelly Fault is variable along its length, being lowest where the fault is modelled as sub-parallel to the Alpine Fault and primarily dextral slip, and higher on sections with strike at a higher angle to the Alpine Fault strike (Fig. 15 A2).

The northern Alpine Fault rupture scenario (Model 2) reaches the Hope-Alpine surface intersection (Fig. 15 B1). This earthquake results in primarily negative stress change on the Hope-Kelly Fault system (Fig. 15 B2). The Alpine Fault south of the source receives positive stress change. The western tips of the Kelly Fault splays receive a patchy pattern of low positive and negative stress change (Fig. 15 B2). The strongest relative negative stress change occurs on the westernmost Hope Fault, where it has normal slip and *E*-W strike, and on the eastern end of the Kelly Fault splays (especially K3 and K4) (Fig. 15 B2).

Model 3 simulates stress change for an earthquake rupturing completely through the intersection; for this scenario we used a constant 5 m displacement on the entire Alpine Fault including extending beyond the intersection zone (Fig. 15 C1). On the Alpine Fault in the centre of the intersection zone, where the fault bends by ~3°, the model has artifacts of positive stress on the Alpine Fault (Fig. 15 C2). Overall, the Hope-Kelly Fault system receives negative stress change from an Alpine Fault earthquake rupturing all the way through the intersection zone

Table 3
Earthquake source rupture parameters used in the CFS modelling.

Results figures	CFS model ID	Source fault	Rupture termination point	Rupture length (km)	Magnitude	Percent slip at surface*	Maximum displacement (m)	Rake	Seismogenic depth (km)
Fig. 15 A1–2	1	central Alpine Fault	North end at Alpine/Kelly southern splay intersection	324	8.1	90	15	168	12
Fig. 15 B1–2	2	northern Alpine Nault	South end at Alpine/westernmost Hope intersection	120	7.4	90	4	166	12
Fig. 15 C1–2	3	Alpine Fault through intersection zone	~20 km north and south of intersection zone	97	–	100	5	168 to 166	15
Fig. 16 A1–3	4	central Hope Fault	Hurunui section to Hope/Kelly branch point at Harper Pass	36	7	70	4	160	12
Fig. 16 B1–3	5	Hope-Kelly Fault (southernmost splay)	Hurunui section to ~10 km east of the Alpine Fault, where Kelly Fault intersects the Alpine Fault at ~10–15 km depth	65	7.3	60	4	160 to 180	12
Fig. 16 C1–3	6	whole Kelly Fault (southernmost splay)	Surface intersection of Alpine/Kelly faults to Harper Pass	62	7.3	60	14	−150 to 180	12

* Chosen based on Dolan and Haravitch (2014), based on estimated cumulative slip of each fault (central Hope fault up to 13 km, Langridge et al., 2014) (Kelly fault <2 km based on Nathan et al., 2002).
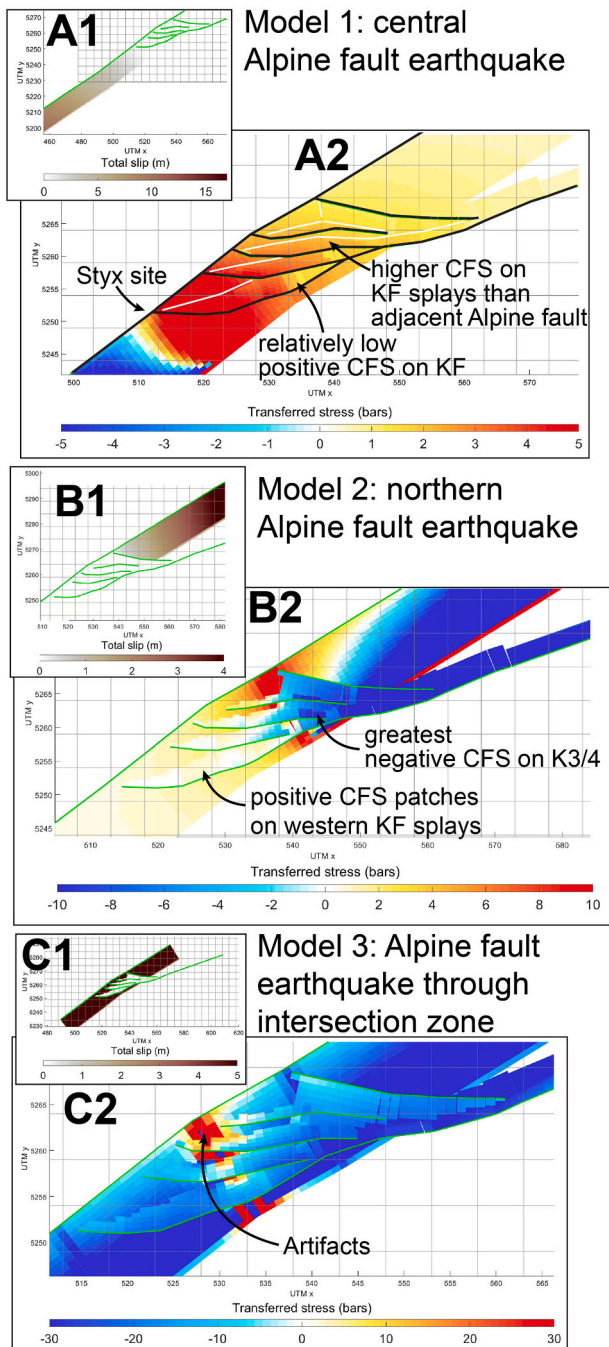
Fig. 15. Coulomb stress transfer modelling results for Alpine fault earthquakes. Source earthquake parameters are listed in Table 3. View in all panels is straight down (map view). A1) Source slip for central Alpine fault earthquake. A2) Coulomb stress transfer from central Alpine fault earthquake. B1) Source slip for south-skewed northern Alpine fault earthquake. B2) Coulomb stress transfer resulting from a northern Alpine fault earthquake. C1) Alpine fault source slip withconstant 5 m slip through the entire intersection zone. C2) Resulting stress transfer. The high stress on the Alpine fault plane at the bend is likely a modelling artifact.

(Fig. 15 C2), though there may be minor regions of positive stress at the base of the Kelly splay faults.

These models overall show that rupture of the central Alpine Fault positively stresses the Hope-Kelly Fault system (Fig. 15 A2). If there was an earthquake on the central Alpine Fault (south of the Hope-Kelly system), this broadly transfers positive CFS to the Hope-Kelly Fault system. This implies that a subsequent earthquake may be triggered on

the Hope-Kelly system. If an earthquake rupture extends through the intersection zone or occurs on the northern Alpine Fault, the Hope-Kelly Faults receive mainly negative stress (Fig. 15 C2). This implies that southward-propagating earthquakes originating on the northern Alpine Fault are expected to inhibit rupture nucleation (i.e., bypass) on the Hope-Kelly system and preferentially continue on to the central Alpine Fault.

5.1.3. Hope-Kelly Fault earthquakes

Three earthquake scenarios (Models 4–6) simulate ruptures on the Hope-Kelly Fault system (Table 3). Model 4 is a central Hope Fault earthquake on the Hurunui section that ends at Harper Pass (Fig. 16 A1). Because of the model resolution and the proximity of the faults, the Hope Fault is not modelled between Michael Creek and Harper Pass (Fig. 16 A1). The Kelly Fault is selected to be the primary structure west of Harper Pass because slip-rates measured in this study show it accommodates most of the slip (Sections 4.3 and 4.5). From this hypothetical earthquake scenario, west of Michael Creek as the Hope and Kelly faults diverge, the Kelly Fault receives greater positive stress than the Hope Fault (Fig. 16 A3). There is a small (<2 bars) positive stress change on the central Alpine Fault and on the southern end of the northern Alpine Fault at depths greater than ~10 km (Fig. 16 A3); above 10 km depth the northern Alpine Fault receives negative CFS.

Model 5 is a Hurunui Hope Fault to central Kelly Fault earthquake (Table 3); this source rupture extends west to ca. 10 km east of the Alpine Fault where the Kelly and Alpine Faults intersect near the base of the seismogenic zone (Fig. 16 B1 and B3). This earthquake scenario produces a positive stress change on the splays of the Kelly Fault of higher magnitude than the western extent of the southern splay (Fig. 16 B3). This suggests that even though the southern splay is often considered the "main splay" of the fault system, the other Kelly Fault splays, and likely the diffuse unmodeled faults, receive high positive stress that may initiate slip on those faults (Fig. 16 B3). The westernmost section of the Hope Fault receives positive stress, but at a much lower magnitude relative to the Kelly splays (Fig. 16 B3). The northern Alpine Fault receives only negative stress, but the central Alpine Fault receives positive stress, especially at depth where it is close to and directly interacting with the slipped fault (Fig. 16 B3).

Model 6 is a complete rupture of the southern splay of the Kelly Fault from Harper Pass to the surface intersection with the Alpine Fault (Table 3, Fig. 16 C1). In the CFS results, the positive stress patches on the source fault are an artifact (Fig. 16 C2 and C3). This earthquake mostly reduces stress on the other Kelly splays and the western Hope Fault, with the exception of a small patch of positive stress near the Hope-Kelly divergence point (Fig. 16 C2). This earthquake produces a large positive stress change on the central Alpine Fault along the intersection (Fig. 16 C3), while the northern Alpine Fault stress is reduced (Fig. 16 C2). This earthquake extends east to Harper Pass, and it produces a positive stress change on the Hurunui segment of the Hope Fault (Fig. 16 C2 and C3).

Combining insights from all three models on the Hope-Kelly Fault system, there is change in the pattern of CFS associated with a change in the proportion of the fault system that ruptures. If an earthquake ruptures the eastern Hope-Kelly Fault up to Michael Creek, the Kelly splays and the central Alpine Fault all experience positive stress (Fig. 16 A2–3 and B2–3). Therefore the earthquake may propagate onto any of the splays. If an earthquake ruptures along the entire length of the southernmost Kelly Fault splay, the rest of the Hope-Kelly Fault system experiences mostly negative stress, but the central Alpine Fault experiences positive stress (Fig. 16 C2–3). Therefore a common feature of earthquake ruptures on the Hope-Kelly Fault system is that the central Alpine Fault is positively stressed.
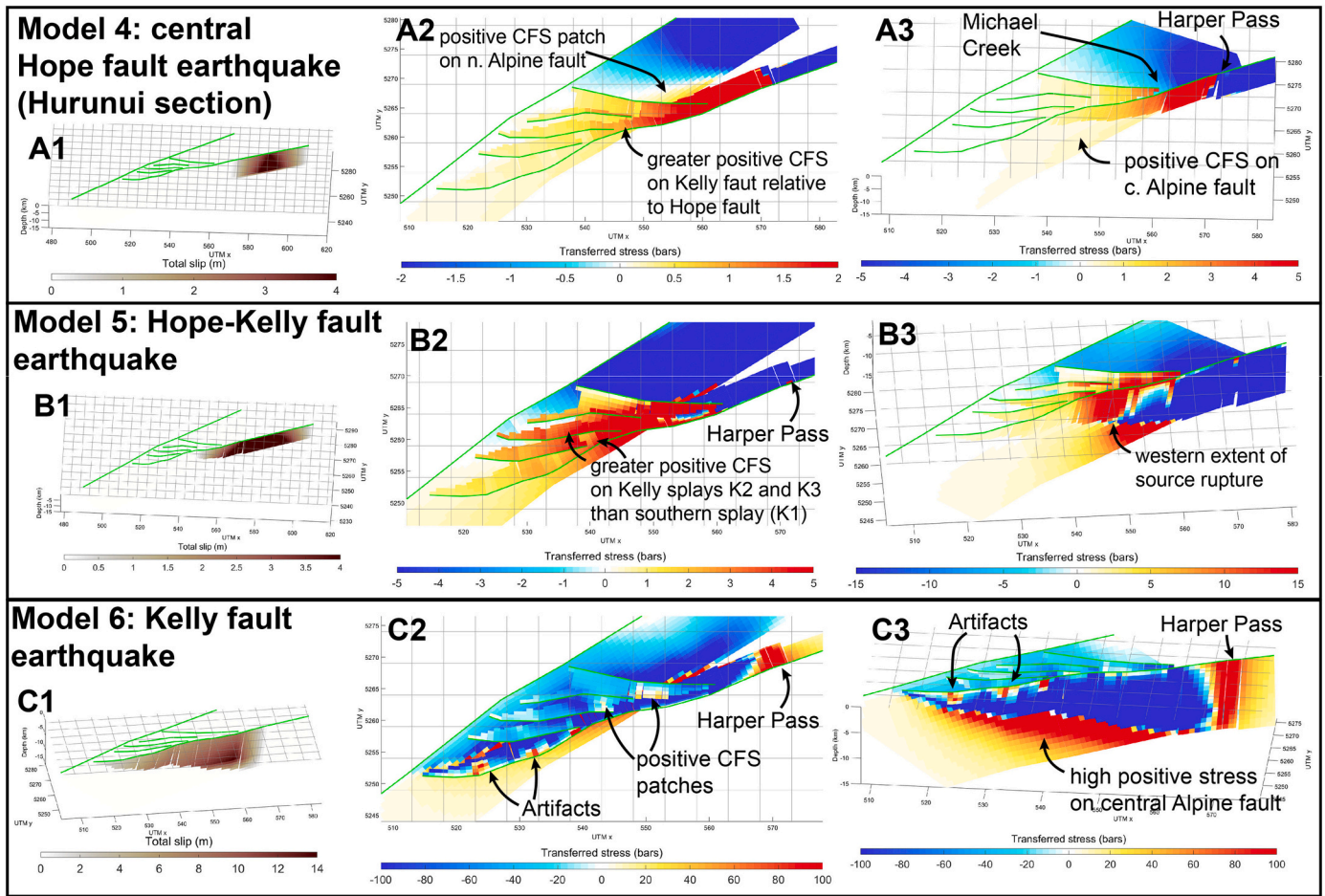
Fig. 16. CFS model results for earthquakes on the Hope-Kelly faults. Source earthquake parameters are listed in Table 3. A1) Slip distribution for the source earthquake on the Hurunui segment of the Hope fault extending west to Harper Pass. A2–3) CFS results for a source earthquake with two different stretch values and model orientation. These panels show the same data just displayed differently. B1) Slip distribution for the Hope-Kelly source earthquake on the Hurunui section of the Hope fault and extending west to ~10 km east of the Alpine Fault surface trace, where the Kelly Fault and Alpine Fault intersect within the seismogenic zone. B2–3) CFS results with two different stretch colours and an oblique view to show the positive stress transfer on the central Alpine fault. These panels show the same data just displayed differently to highlight different aspects of the CFS pattern. C1) Source earthquake slip distribution for a full Kelly southern splay rupture. Model orientation is the same as panel C3. C2–3) CFS results of the Kelly fault source earthquake. These panels show the same data just displayed differently. The patches of positive stress on the source fault are artifacts.

6. Discussion

6.1. Slip-rate variations through the Hope-Kelly Fault system: discrete and distributed strain in an incipient fault interaction zone

The estimated slip-rates for the Hope and Kelly faults are highly variable, between 1 and >6 mm/yr over a distance spanning only ~15 km along strike, highlighting the complexity of the fault system. Overall, the Kelly Fault has a faster late Quaternary slip-rate than the westernmost Hope Fault. In the area studied here, the Hope and Kelly principal slip zones are close together (within 1–5 km perpendicular to strike, across the valley) and both have a discontinuous mappable surface trace, with many other low displacement, short faults mapped in the distributed deformation zone. There could be un-measured slip on structures between and around the principal slip zone segments where we have measured slip-rates; distributed deformation within complex and young fault systems is anticipated (Dolan and Haravitch, 2014; Zinke et al., 2014).

To infer how much unrecognized slip may be within the Hope-Kelly Fault system, we use horizontal slip vector balancing with the surrounding faults, according to the methods of Langridge et al. (2010) and Vermeer et al. (2021). In this process only one slip vector measurement

or an average slip vector should be used from each fault in the system, and slip vectors from parallel faults should be added to capture the slip across the whole width of the fault system. In this case we use the Locke Stream slip-rate for the Kelly Fault (Section 4.3 Site 3, 6.2 (+2.7/−1.4) mm/yr) and the Yeo Creek measurement for the Hope Fault (Section 4.2 Site 2, 5.6 (+2.1/−0.7) mm/yr) (Fig. 17A). Alternatively, the rate from KF3 (west of Sackung Hill) could be used alone, since at this point in the fault system much of the dextral slip from the Hope Fault has been transferred onto the Kelly Fault (see Section 4.6 for discussion of Hope-Kelly linking faults exposed on Sackung Hill). Compared to the average slip vector on the Hurunui segment (Khajavi et al., 2018), the Hope and Kelly faults have a combined horizontal slip vector that is within error of the Hurunui average slip vector (Fig. 17 B). However, the average Hurunui section slip vector is determined at sites east of the Hurunui-Kakapo fault intersection, so it may be an underestimate of the slip-rate on the western Hurunui section which turns into the Hope-Kelly Fault system (Khajavi et al., 2018). Slip-rate estimates at Harper Pass are ~15 mm/yr (Hardy and Wellman, 1984; Langridge et al., 2003). The slip-vector balancing in Langridge et al. (2010) used McKenzie Fan on the Hurunui section (Fig. 1, location E), plus the eastern Kakapo fault (Fig. 1, location L) slip vectors to balance with the central to northern Alpine Fault slip vector change (Fig. 1, locations A and C). We
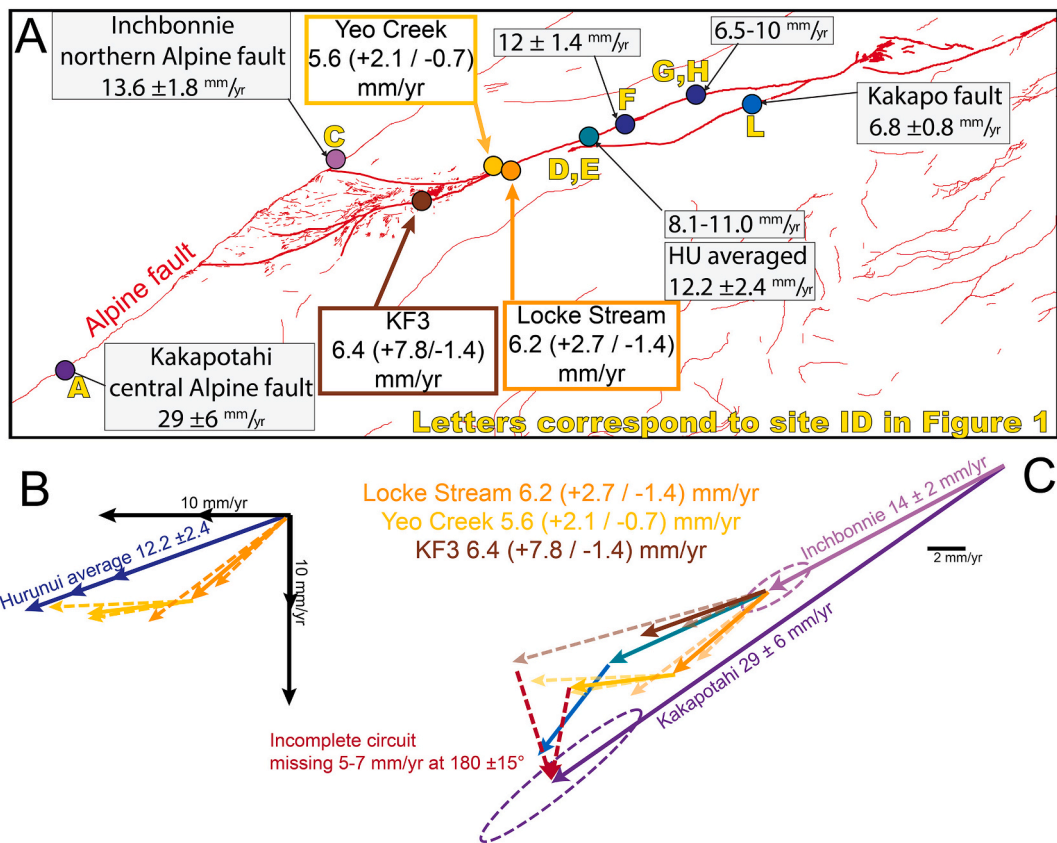
Fig. 17. Slip circuits. A) Map showing the slip-rate measurements on the Alpine fault and Hope fault. B) The combined horizontal slip vectors from Locke Stream and Yeo Creek in the Hope-Kelly fault system are within error of the average eastern Hurunui section HSV. C) The Alpine fault HSV from the central and northern sections, taken from slip-rates at Kakapotahi and Inchbonnie and assuming fault dip of 50 degrees (Norris and Cooper, 2001; Langridge et al., 2010). The eastern Hurunui average HSV (Khajavi et al., 2018), and the combined Yeo and Lock slip vectors, all fall short of completing the Alpine fault slip decrease. The missing HSV is 5–7 mm/yr at 180 ± 15°.

subsequently compare the slip vectors measured in the Hope-Kelly Fault system to the slip vector change on the Alpine Fault (Fig. 17 C). We expect that all the deformation in the Hope-Kelly Fault system on the combined vectors would fill the gap between the central Alpine Fault and northern Alpine Fault slip vectors. However, the slip vectors we have measured do not entirely fill the gap. There is 5–7 mm/yr at 180 ± 15° unaccounted for (Fig. 17). The missing slip may be accommodated on structures without surface expression appropriate for making slip-rate measurements or distributed among many low displacement structures.

Estimated slip-rates are based on displaced early post-glacial to early Holocene landforms, with total slip accumulated over 7–16 kyr. Most of the slip-rate measurements on the central Hope Fault and Alpine Fault are from displaced late Holocene landforms <5 kyr (see references in Fig. 1). Studies on the Hope Fault and other MFS faults have shown that slip-rates on single fault segments or at single sites covering different time windows vary through time (Gold and Cowgill, 2011; Khajavi et al., 2018; Zinke et al., 2019; Hatem et al., 2020; Zinke et al., 2021). This temporal variability in slip-rates may be an additional factor in why the 7–16 ka Hope-Kelly slip vectors from this study are in deficit to the central-northern Alpine Fault slip-rate change, and do not balance like the late Holocene Alpine-Hope-Kakapo slip circuit.

6.2. Timing of last surface rupture on the Hope-Kelly Fault relative to adjacent fault segments and Alpine Fault earthquakes

The paleoseismic trenching (Section 4.1.2) and dating of possible shaking proxies (damming of Lake Kaurapataka and tree death, Appendix D) provide preliminary constraints on the timing of the most

recent surface rupturing earthquake on the Hope-Kelly Fault system. The 14C date in faulted sediment on the Hope Fault at Site 1: Michael Creek constrains the age of surface rupture to between ca. 1650–1840 CE, the lower bound being the maximum possible age of the dated material, and the upper bound being constrained by widespread European settlement and the absence of a large earthquake being recorded. The trench and subsequent 14C sampling did not provide sufficient stratigraphy and material to constrain this age further; the wide age range is a consequence of the flat shape of the 14C calibration curve around the time interval in question. However, assuming the sedimentation forming the fan that dammed Lake Kaurapataka was due to proximal strong shaking, the death age of the tree indicates that the earthquake occurred in the early 1800's. Indicators of strong shaking have also been recognized in Lake Kaniere, east of the Alpine Fault, near Site 8: Styx, which is dated at 1809–1880 CE (Howarth et al., 2021). This has been connected to the proposed post-1717 surface rupture dated at 1813–1848 CE on the Alpine Fault in paleoseismic trenches at Staples (Fig. 1, site B), just south of the Site 8: Styx River (Langridge et al., 2020). Finally, there is no post-European colonization historic record of a strong earthquake in this region, limiting the minimum age to before ~1840.

Langridge et al. (2020) attributed the early 1800's Alpine Fault surface rupture at Staples (Fig. 1 site B) to either a short partial section rupture of the Alpine Fault, or triggered slip from an earthquake primarily on the Hope-Kelly Faults. Preliminary data is consistent with the latter interpretation, however it is not conclusive. The isoseismals for a M 7.4 northern Alpine Fault earthquake presented by Langridge et al. (2020) have strong shaking overlap with the Lake Kaurapataka area, so increased sedimentation caused by strong shaking there may not be exclusively triggered by Hope-Kelly earthquakes but also Alpine Fault

earthquakes. To explain the shaking proxies and surface rupture observations along the Alpine Fault, Langridge et al. (2020) preferred the interpretation that the early 1800's Alpine Fault surface rupture was from an earthquake primarily on the Kelly Fault which triggered Alpine Fault slip with a limited spatial extent. This scenario is within the possible interpretations of the Hope-Kelly Fault earthquake dating. However, considered without shaking proxies, the depositional age of faulted sediments at Site 1: Michael Creek does not constrain the age of the surface rupture with enough certainty to determine whether it was co-seismic with ruptures on other proximal faults in the Alpine-Hope-Kelly Fault region during the ~200 year interval between 1650 and 1840.

6.3. Stress modelling and fault interactions

As indicated from CFS modelling, earthquakes on the central Alpine Fault could exert up to 10 bars of positive Coulomb stress on parts of the Hope-Kelly Fault system. However, ruptures on the Alpine Fault which pass completely through the intersection zone and earthquakes limited to the northern Alpine Fault both decrease Coulomb stress on most of the Hope-Kelly Fault system. Earthquakes on the southern Kelly Fault splay substantially decrease Coulomb stress on the northern Alpine Fault but could impart large (>20 bars) positive stress change on the central Alpine Fault. Earthquakes on the southern Kelly Fault splay also impart positive stress on the Hurunui section of the Hope Fault, and vice-versa. These patterns of stress interaction suggest that the Hope-Kelly Fault system is a stress-efficient link between the central Alpine Fault and the Hope Fault. The magnitude of positive stress changes modelled in many of the rupture scenarios investigated herein exceed the estimates of threshold triggering Coulomb stress changes estimated from other scenarios. A Coulomb stress increase of 0.01 MPa (0.1 bar) is commonly proposed to be the threshold for potential earthquake triggering (Harris, 1998; Reasenberg and Simpson, 1997; Freed, 2005; King et al., 1994; Stein, 1999), although Coulomb stress changes of >0.1 MPa (Zhan et al., 2011) and 1 to 1.5 MPa (Walters et al., 2018) were insufficient to generate spontaneous rupture during the 2010–2011 Canterbury earthquake sequence and 2016 Central Italy seismic sequence, respectively. Mohammadi et al. (2019) estimated a Coulomb stress change threshold sufficient to trigger receiver fault rupture of ca. 1 to 4 bars based on an analysis of global events.

The location of the central-northern Alpine Fault section boundary was primarily determined by the slip-rate change and the presence of the Hope-Kelly-Alpine intersection that marks the southern extent of the MFS. Although there is a slight bend in the Alpine Fault within the Hope-Kelly intersection zone, there is no recognized geometric feature in this region on the Alpine Fault large enough to stop an earthquake rupture, according to global databases of strike-slip fault complexities (e.g. Wesnousky, 2006; Lozos, 2021; Elliott et al., 2015; Biasi and Wesnousky, 2016; Biasi and Wesnousky, 2017; Elliott et al., 2018). However, this CFS modelling shows the Hope-Kelly Fault system may impart a complex stress pattern on the Alpine Fault. If a northward propagating rupture on the central Alpine Fault was sufficient to trigger slip on the Kelly Fault splays at the same time as the continuation of the Alpine Fault rupture, the interaction of static stresses would be complex. Slip on the central Alpine Fault positively stresses the northward continuation of the Alpine Fault through the intersection zone but slip on the southern Kelly splay causes negative stress on the Alpine Fault plane north of the ruptured portion of the Kelly Fault. Depending on the relative stresses, pre-stresses, and other dynamic factors not captured by this modelling, it is conceivable that the Hope-Kelly-Alpine intersection could arrest a northward propagating central Alpine Fault rupture by producing competing stresses on the Alpine Fault plane within the intersection zone.

Ruptures on the Hope-Kelly Fault system cause negative CFS on the northern Alpine Fault. The other MFS faults may exert a similar pattern of positive stress change south of the intersection and negative stress

change north of the intersection. This complex spatial and temporal patchwork of stress change exerted on the northern Alpine Fault could make the behaviour of the fault spatially and temporarily heterogeneous. Paleoseismic work on the northern Alpine Fault has not resulted in well-accepted precise age distributions and rupture extents of Holocene earthquakes (Yetton, 1998). At this stage, we can conclude that Coulomb stress changes associated with northern and central Alpine Fault earthquakes generate distinct patterns on the Hope-Kelly receiver faults that may be important in dictating rupture propagation onto adjacent parts of the Alpine Fault and the Hope-Kelly Fault system.

The transfer of coseismic Coulomb stresses between the Alpine and Hope-Kelly Faults could affect the millennial-scale pattern of earthquakes, slip-rates and recurrence intervals of all the faults involved. Work on the central and southern sections of the Alpine Fault show it may exhibit diverse rupture modes that could vary over 5–10 kyr timescales when it preferentially stops at the central-southern section boundary vs propagates through it (De Pascale et al., 2014; Howarth et al., 2021). If this behaviour also holds true at the central-northern section boundary, when the Alpine Fault is in central-northern dual-section mode it would repeatedly rupture through the section boundary and decrease stress on the Hope-Kelly Fault system. Inversely, when the Alpine Fault is in single-section mode, central section earthquakes would repeatedly stop near the central-northern boundary and impart positive Coulomb stress on the Hope-Kelly Fault system. While less frequent and/or lower displacement (due to lower slip-rate) northern section earthquakes may alternately decrease the stress, overall, the Alpine Fault in single-section rupture mode would likely produce a net increase in Coulomb stress and promote more frequent ruptures of the Hope-Kelly Faults. This could in turn promote more frequent rupture of the Hurunui section of the Hope Fault. If this pattern persisted over multiple earthquake cycles, the 5–10 kyr slip-rate on the Hope-Kelly system and potentially the Hurunui segment during that time would be faster than the long-term average. Alternatively, when the Alpine Fault is in a dual-section rupture mode, each rupture through the intersection zone and onto the northern Alpine Fault would decrease the Coulomb stress on the Hope-Kelly Fault system. The repeated negative CFS may impede rupture nucleation, potentially increasing recurrence intervals and decreasing slip-rate on the Hope-Kelly Fault system while the Alpine Fault is in dual-section mode. Future work understanding the tendency for single vs dual-section ruptures of the central to northern Alpine Fault should include the effects of the stress transfer interactions with the MFS faults. Also, partial section rupture of the northern Alpine Fault may be promoted by stress interactions at each of the MFS intersections.

6.4. Implications for seismic hazard and plate boundary faulting mechanics

The slip-rates presented here are the first for the Hope-Kelly Fault system and the western Hope Fault. In the eastern part of the fault system, the Hope and Kelly faults are close together and interact within the upper 5 km of crust. As they diverge, the Hope Fault slip-rate decreases to <2 mm/yr of dextral slip, while the Kelly Fault maintains a minimum of 6.2 (+7.8/−1.2) mm/yr. Up to 7 mm/yr of slip (up to 50% of expected slip) is unaccounted for in HSV balancing with the Alpine Fault, indicating that slip distributed onto low displacement and/or unrecognized faults likely plays an important role in this intersection zone.

Coulomb stress transfer modelling using the 3D fault geometry shows that the central Alpine Fault, Kelly Fault, and Hurunui section of the Hope Fault form a kinematically efficient stress-transfer zone. Central Alpine Fault earthquakes almost equivalently increase Coulomb stress on the Kelly Fault splays and northern continuation of the Alpine Fault. If CFS is the main factor in determining fault behaviour, central Alpine Fault ruptures could be expected to cascade either onto the Hope-Kelly Faults and/or continue on the northern Alpine Fault with roughly

equivalent probability. This is congruent with the observation that approximately 50% of the central Alpine Fault slip continues onto the northern Alpine Fault, and the other 50% is transferred through the intersection onto the central Hope Fault, as inferred from slip-rates (Langridge et al., 2010). Meanwhile, the repeated negative CFS exerted on the northern Alpine Fault by Hope-Kelly ruptures may repeatedly inhibit rupture nucleation on that section. This pattern of stress may be similar at each MFS-Alpine Fault intersection, potentially causing spatial and temporal variations in rupture behaviours of the northern Alpine Fault. Coulomb stress modelling provides a mechanism that would encourage spatiotemporal clustering of earthquakes in the Alpine - Hope - Kelly Fault system. Alternative mechanisms not addressed here include clustering due to dynamic stresses (Belardinelli et al., 2003) and potential influences of megathrust rupture cycling on upper plate faulting (Lamb et al., 2018).

7. Conclusions

1. The Hope Fault slip-rate decreases westward from 5.6 ($+2.1/-0.7$) mm/yr to 1.7 ($+1.1/-0.4$) mm/yr. West of this point the Hope Fault strike bends to $090 \pm 10°$ and there is no unambiguous surface expression of the fault.
2. The Kelly Fault has variable slip-rate along its length, with a maximum measured slip-rate of 6.2 ($+7.8/-1.2$) mm/yr at Site 5: KF3. Because the landforms may be younger than inferred, this slip-rate should be considered a minimum. Because of the higher slip-rate compared to the Hope Fault, we consider the Kelly Fault to be the principal fault in the central and eastern parts of the Hope-Kelly Fault system.
3. 14C dating of faulted sediments on the Hope Fault (Site 1: Michael Creek) and shaking proxies (Appendix D) constrain the most recent surface rupture in the Hope-Kelly Fault system to between 1653 and 1848 CE.
4. Horizontal slip vector balancing shows that the new slip-rates on the Hope and Kelly faults match the average slip-rate of the eastern Hurunui segment of the Hope Fault but fall short of accounting for all the slip-rate transferred off the Alpine Fault across the intersection zone (Langridge et al., 2010). The missing 5–7 mm/yr of strain may be accommodated by distributed deformation on small and/or unrecognized faults within this complex and diffuse fault system.
5. CFS modelling shows that the Hope-Kelly Fault system is a stress-efficient link between the central Alpine Fault and the central Hope Fault. A central Alpine Fault rupture induces roughly equal CFS onto the northern Alpine Fault and the Kelly Fault splays. Repeated over many seismic cycles, this provides a mechanism for transferring central Alpine Fault slip onto the Hope Fault via cascading or triggered Hope-Kelly ruptures. Meanwhile, rupture of the Hope-Kelly Faults decreases Coulomb stress on the northern Alpine Fault, potentially impeding the seismic cycle of the northern Alpine Fault, increasing the time to the next rupture and decreasing the northern Alpine Fault slip-rate if this continues over many seismic cycles. The negative CFS transfer between the northern Alpine Fault and Hope-Kelly Faults also suggests it is unlikely for these fault sections to trigger rupture on each other. These findings are significant for both understanding fault behaviour over multiple seismic cycles, and for earthquake hazards posed by these major plate boundary faults.

CRediT authorship contribution statement

Jessie L. Vermeer: Conceptualization, Methodology, Investigation, Writing – original draft, Writing – review & editing, Visualization, Data curation, Project administration. **Mark C. Quigley:** Conceptualization, Methodology, Investigation, Resources, Writing – original draft, Writing – review & editing, Supervision, Funding acquisition. **Robert M. Langridge:** Conceptualization, Methodology, Investigation, Resources, Writing – original draft, Writing – review & editing, Supervision,

Funding acquisition. **Brendan G. Duffy:** Conceptualization, Methodology, Investigation, Writing – review & editing, Supervision. **Zoë K. Mildon:** Conceptualization, Methodology, Software, Investigation, Resources, Writing – review & editing, Data curation. **Manuel-Lukas Diercks:** Methodology, Software, Writing – review & editing.

Declaration of Competing Interest

The authors declare that they have no known competing financial interests or personal relationships that could have appeared to influence the work reported in this paper.

Data availability

All data is available in the text, appendices, or cited references.

Appendix. Supplementary data

Supplementary data to this article can be found online at https://doi.org/10.1016/j.tecto.2022.229593.

References

Allen, S., Cox, S., Owens, I., 2011. Rock avalanches and other landslides in the central Southern Alps of New Zealand : a regional study considering possible climate change impacts. Landslides 8, 33–48. https://doi.org/10.1007/s10346-010-0222-z.

Barnes, Audru, 1999. Recognition of active strike-slip faulting from high-resolution marine seismic reflection profiles: Eastern Marlborough fault system, New Zealand. Geol. Soc. Am. Bull. 111 (4), 538–559. https://doi.org/10.1130/0016-7606(1999)111<0538:ROASSF>2.3.CO;2.

Barrell, D.J.A., Andersen, B., Denton, G., 2011. Glacial geomorphology of the central South Island, New Zealand. In: GNS Science Monograph, 27. http://shop.gns.cri.nz/mon27/.

Barrows, T.T., Almond, P., Rose, R., Fi, L.K., Mills, S.C., Tims, S.G., 2013. Late Pleistocene Glacial Stratigraphy of the Kumara-Moana region, West Coast of South Island, New Zealand, 74. https://doi.org/10.1016/j.quascirev.2013.04.010.

Barth, N.C., Boulton, C., Carpenter, B.M., Batt, G.E., Toy, V.G., 2013. Slip localization on the southern Alpine Fault, New Zealand. Tectonics 32 (3), 620–640. https://doi.org/10.1002/tect.20041.

Belardinelli, M.E., Bizzarri, A., Cocco, M., 2003. Earthquake triggering by static and dynamic stress changes. J. Geophys. Res. 108, 2135. https://doi.org/10.1029/2002JB001779, B3.

Biasi, G.P., Wesnousky, S.G., 2016. Steps and gaps in ground ruptures: Empirical bounds on rupture propagation. Bull. Seismol. Soc. Am. 106, 1110–1124. https://doi.org/10.1785/0120150175.

Biasi, G.P., Wesnousky, S.G., 2017. Bends and ends of surface ruptures. Bull. Seismol. Soc. Am. v. 107, 2543–2560. https://doi.org/10.1785/0120160292.

Berryman, K.R., Beanland, S., Cooper, A.F., Cutten, H.N., Norris, R.J., Wood, P.R., 1992. The Alpine Fault, New Zealand: variation in Quaternary style and geomorphic expression. Annales Tectonicae 6, 126–163.

Bronk Ramsey, C., 2009. Bayesian analysis of radiocarbon dates. Radiocarbon 51 (1), 337–360.

Brown, N., 2020. Which geomorphic processes can be informed by luminescence measurements? Geomorphology 367. https://doi.org/10.1016/j.geomorph.2020.107296.

Cochran, U.A., Clark, K.J., Howarth, J.D., Biasi, G.P., Langridge, R.M., Villamor, P., Berryman, K.R., Vandergoes, M.J., 2017. A plate boundary earthquake record from a wetland adjacent to the Alpine Fault in New Zealand refines hazard estimates. Earth Planet. Sci. Lett. v. 464, 175–188. https://doi.org/10.1016/j.epsl.2017.02.026.

Cowan, H.A., 1990. Late Quaternary displacements on the Hope Fault at Glynn Wye, North Canterbury. New Zealand J. Geol. Geophys. 33 (2), 285–293. https://doi.org/10.1080/00288306.1990.10425686.

Cowan, H., McGlone, M., 1991. Late Holocene displacements and characteristic earthquakes on the Hope River segment of the Hope Fault, New Zealand. J. Royal Soc. New Zealand 21 (4), 373–384. https://doi.org/10.1080/03036758.1991.10420834.

Cowgill, E., 2007. Impact of riser reconstructions on estimation of secular variation in rates of strike-slip faulting: Revisiting the Cherchen River site along the Altyn Tagh Fault, NW China. Earth Planet. Sci. Lett. 254, 239–255. https://doi.org/10.1016/j.epsl.2006.09.015.

De Pascale, G.P., Quigley, M.C., Davies, T.R.H., 2014. Lidar reveals uniform Alpine Fault offsets and bimodal plate boundary rupture behavior, New Zealand. Geology 42, 411–414. https://doi.org/10.1130/G35100.1.

Dolan, J.F., Haravitch, B.D., 2014. How well do surface slip measurements track slip at depth in large strike-slip earthquakes? The importance of fault structural maturity in controlling on-fault slip versus off-fault surface deformation. Earth Planet. Sci. Lett. 388, 38–47. https://doi.org/10.1016/j.epsl.2013.11.043.

Dolan, J.F., Bowman, D.D., Sammis, C.G., 2007. Long-Range and Long-Term Fault Interactions in, vol. 35. Geology, Southern California, pp. 855–858. https://doi.org/10.1130/G23789A.1.

Dolan, J.F., Mcauliffe, L.J., Rhodes, E.J., Mcgill, S.F., Zinke, R.W., 2016. Extreme multi-millennial slip-rate variations on the Garlock fault, California : Strain super-cycles, potentially time-variable fault strength, and implications for system-level earthquake occurrence. Earth Planet. Sci. Lett. 446, 123–136. https://doi.org/10.1016/j.epsl.2016.04.011.

Eaves, S.R., Anderson, B.M., Mackintosh, A.N., 2017. Glacier-based climate reconstructions for the last glacial-interglacial transition: Arthur's Pass, New Zealand (43°S). J. Quat. Sci. 32, 877–887. https://doi.org/10.1002/jqs.2904.

Elliott, A.J., Oskin, M.E., Liu-Zeng, J., Shao, Y., 2015. Rupture termination at restraining bends: the last great earthquake on the Altyn Tagh Fault. Geophys. Res. Lett. 42, 2164–2170. https://doi.org/10.1002/2015GL063107.

Elliott, A.J., Oskin, M.E., Liu-zeng, J., Shao, Y.X., 2018. Persistent rupture terminations at a restraining bend from slip-rates on the eastern Altyn Tagh fault. Tectonophysics 733, 57–72. https://doi.org/10.1016/j.tecto.2018.01.004.

Freed, A.M., 2005. Earthquake triggering by static, dynamic, and postseismic stress transfer. Annu. Rev. Earth Planet. Sci. 33, 335–367. https://doi.org/10.1146/annurev.earth.33.092203.122505.

Freund, R., 1971. Hope Fault a Strike Slip Fault in New Zealand. New Zealand Geol. Surv. Bull. 16 (1).

Gauriau, J., Dolan, J.F., 2021. Relative structural complexity of plate-boundary fault systems controls incremental slip-rate behavior of major strike-slip faults. Geochem. Geophys. Geosyst. 22, 1–24. https://doi.org/10.1029/2021GC009938.

Gold, R.D., Cowgill, E., 2011. Deriving fault-slip histories to test for secular variation in slip, with examples from the Kunlun and Awatere faults. Earth Planet. Sci. Lett. 301, 52–64. https://doi.org/10.1016/j.epsl.2010.10.011.

Hardy, E.F., Wellman, H.W., 1984. The Alpine, Wairau & Hope Faults. Victoria University of Wellington, Geology Department.

Harris, R.A., 1998. Forecasts of the 1989 Loma Prieta, California, earthquake. Bull. Seismol. Soc. Am. 88, 898–916.

Harris, R.A., Simpson, R.W., Reasenberg, P.A., 1995. Influence of static stress changes on earthquake locations in southern California. Nature 375, 221–224. https://doi.org/10.1038/375221a0.

Hatem, A.E., Dolan, J.F., Zinke, R.W., Langridge, R.M., McGuire, C.P., Rhodes, E.J., Brown, N., Van Dissen, R.J., 2020. Holocene to latest Pleistocene incremental slip-rates from the east-Central Hope Fault (Conway segment) at Hossack Station, Marlborough fault system, South Island, New Zealand: towards a dated path of earthquake slip along a plate boundary fault. Geosphere 16, 1–27. https://doi.org/10.1130/ges02263.1.

Hogg, A.G., Heaton, T.J., Hua, Q., Palmer, J.G., Turney, C.S.M., Southon, J., Bayliss, A., Blackwell, P.G., Boswijk, G., Bronk Ramsey, C., Pearson, C., Petchey, F., Reimer, P., Reimer, R., et al., 2020. SHCal20 Southern hemisphere calibration, 0-55,000 years cal BP. Radiocarbon v. 62, 759–778. https://doi.org/10.1017/RDC.2020.59.

Holm, K., Bovis, M., Jakob, M., 2004. The landslide response of alpine basins to post-Little Ice Age glacial thinning and retreat in southwestern British Columbia. Geomorphology 57, 201–216. https://doi.org/10.1016/S0169-555X(03)00103-X.

Hormes, A., Preusser, F., Denton, G., Hajdas, I., Weiss, D., Stocker, T.F., Schlüchter, C., 2003. Radiocarbon and luminescence dating of overbank deposits in outwash sediments of the last Glacial Maximum in North Westland, New Zealand. N. Z. J. Geol. Geophys. 46, 95–106. https://doi.org/10.1080/00288306.2003.9514998.

Howarth, J.D., Cochran, U.A., Langridge, R.M., Clark, K., Fitzsimons, S.J., Berryman, K., Villamor, P., Strong, D.T., 2018. Past large earthquakes on the Alpine Fault: paleoseismological progress and future directions. N. Z. J. Geol. Geophys. 61, 309–328. https://doi.org/10.1080/00288306.2018.1464658.

Howarth, J.D., Barth, N.C., Fitzsimons, S.J., Richards-Dinger, K., Clark, K.J., Biasi, G.P., Cochran, U.A., Langridge, R.M., Berryman, K.R., 2021. Spatiotemporal clustering of great earthquakes on a transform fault controlled by geometry. Nat. Geosci. 14, 314–320. https://doi.org/10.1038/s41561-021-00721-4.

Hughes, A., Bell, R.E., Mildon, Z.K., Rood, D.H., Whittaker, A.C., Rockwell, T.K., Levy, Y., DeVecchio, D.E., Marshall, S.T., Nicholson, C., 2020. Three-dimensional structure, ground rupture hazards, and static stress models for complex nonplanar thrust faults in the Ventura Basin, Southern California. J. Geophys. Res. Solid Earth 125. https://doi.org/10.1029/2020JB019539.

Kearse, J., Little, T.A., Van Dissen, R.J., Barnes, P.M., Langridge, R.M., Mountjoy, J., Ries, W., Villamor, P., Clark, K.J., Benson, A., Lamarche, G., Hill, M., Hemphill-Haley, M., 2018. Onshore to offshore ground-surface and seabed rupture of the Jordan–Kekerengu–Needles fault network during the 2016 Mw 7.8 Kaikoura Earthquake, New Zealand. Bull. Seismol. Soc. Am. 108, 1573–1595. https://doi.org/10.1785/0120170304.

Khajavi, N., Langridge, R.M., Quigley, M.C., Smart, C., Rezanejad, A., Martín-González, F., 2016. Late Holocene rupture behavior and earthquake chronology on the Hope Fault, New Zealand. Geol. Soc. Am. Bull. 128, 1736–1761. https://doi.org/10.1130/B31199.1.

Khajavi, N., Nicol, A., Quigley, M.C., Langridge, R.M., 2018. Temporal slip-rate stability and variations on the Hope Fault, New Zealand, during the late quaternary. Tectonophysics 738–739, 112–123. https://doi.org/10.1016/j.tecto.2018.05.001.

King, G.C.P., Stein, R.S., Lin, Jian, 1994. Static stress changes and the triggering of earthquakes. Bull. Seismol. Soc. Am. 84, 935–953. https://doi.org/10.1016/0148-9062(95)94484-2.

Kos, Amann, Strozzi, Delaloye, Ruette, Springman, 2016. Contemporary glacier retreat triggers a rapid landslide response, Great Aletsch Glacier, Switzerland. Geophys. Res. Lett. 43 (24), 12466–12474. https://doi.org/10.1002/2016GL071708.

Lamb, S., Arnold, R., Moore, J.D.P., 2018. Locking on a megathrust as a cause of distributed faulting and fault-jumping earthquakes. Nat. Geosci. https://doi.org/10.1038/s41561-018-0230-5.

Langridge, R.M., Campbell, J.K., Hill, N., Pere, V., Pope, J., Pettinga, J.R., Estrada, B., Berryman, K., 2003. Paleoseismology and slip-rate of the Conway Segment of the Hope Fault at Greenburn Stream, South Island, New Zealand. Ann. Geophys. 46, 1119–1140. https://doi.org/10.4401/ag-3449.

Langridge, R.M., Villamor, P., Basili, R., Almond, P., Martinez-Diaz, J.J., Canora, C., 2010. Revised slip-rates for the Alpine Fault at Inchbonnie: implications for plate boundary kinematics of South Island, New Zealand. Lithosphere 2, 139–152. https://doi.org/10.1130/L88.1.

Langridge, R.M., Ries, W.F., Farrier, T., Barth, N.C., Khajavi, N., De Pascale, G.P., 2014. Developing sub 5-m LiDAR DEMs for forested sections of the Alpine and Hope Faults, South Island, New Zealand: Implications for structural interpretations. J. Struct. Geol. 64, 53–66. https://doi.org/10.1016/j.jsg.2013.11.007.

Langridge, R.M., Ries, W., Litchfield, N., Villamor, P., Van Dissen, R.J., Barrell, D., Rattenbury, M., Heron, D., Haubrock, S., Townsend, D., Lee, J., Berryman, K., Nicol, A., Cox, S., et al., 2016. The New Zealand active faults database. N. Z. J. Geol. Geophys. 59, 86–96. https://doi.org/10.1080/00288306.2015.1112818.

Langridge, R.M., Ries, W.F., Dolan, J.F., Schermer, E.R., Siddoway, C., 2017. Slip rate estimates and slip gradient for the Alpine Fault at Calf Paddock, Maruia River, New Zealand. N. Z. J. Geol. Geophys. 60, 73–88. https://doi.org/10.1080/00288306.2016.1275707.

Langridge, R.M., Villamor, P., Howarth, J.D., Ries, W.F., Clark, K.J., Litchfield, N.J., 2020. Reconciling an Early Nineteenth-Century Rupture of the Alpine Fault at a Section End, Toaroha River, Westland, New Zealand. Bulletin of the Seismological Society of America. https://doi.org/10.1785/0120200116.

Litchfield, N.J., Van Dissen, R.J., Sutherland, R., Barnes, P.M., Cox, S.C., Norris, R., Beavan, R.J., Langridge, R., Villamor, P., Berryman, K., Stirling, M., Nicol, A., Nodder, S., Lamarche, G., et al., 2014. A model of active faulting in New Zealand. N. Z. J. Geol. Geophys. 57, 32–56. https://doi.org/10.1080/00288306.2013.854256.

Litchfield, N.J., Villamor, P., van Dissen, R.J., Nicol, A., Barnes, P.M., Barrell, D.J.A., Pettinga, J.R., Langridge, R.M., Little, T.A., Mountjoy, J.J., Ries, W.F., Rowland, J., Fenton, C., Stirling, M.W., et al., 2018. Surface rupture of multiple crustal faults in the 2016 Mw 7.8 Kaikōura, New Zealand, earthquake. Bull. Seismol. Soc. Am. 108, 1496–1520. https://doi.org/10.1785/0120170300.

Little, Van Dissen, Kearse, Norton, Benson, Wang, 2018. Kekerengu fault, New Zealand: timing and size of Late Holocene surface ruptures. Bull. Seismolog. Soc. Am. https://doi.org/10.1785/0120170152.

Lozos, J.C., 2021. The effect of along-strike variation in dip on rupture propagation on strike-slip faults, 17, pp. 1–15. https://doi.org/10.1130/GES02391.1/5455696/ges02391.pdf.

Mackenzie, D., Elliott, A.J., 2017. Untangling tectonic slip from the potentially misleading effects of landform geometry. Geosphere 13, 1310–1328. https://doi.org/10.1130/GES01386.1.

Maon, 2006. Rates of active faulting during late Quaternary fluvial terrace formation at Saxton River, Awatere fault, New Zealand. Geol. Soc. Am. Bull. 118 (11–12), 1431–1446. https://doi.org/10.1130/B25961.1.

McKay, A., 1890. On the earthquakes of September 1888 in the Amuri and Marlborough districts of the South Island: New Zealand. Geol. Surv. Rep. Geol. Explor. 20, 1–16.

Mildon, Z.K., Toda, S., Faure Walker, J.P., Roberts, G.P., 2016. Evaluating models of Coulomb stress transfer: is variable fault geometry important? Geophys. Res. Lett. 43, 12,407–12,414. https://doi.org/10.1002/2016GL071128.

Mohammadi, H., Quigley, M.C., Steacy, S., Duffy, B., 2019. Effects of source model variations on Coulomb stress analyses of a multi-fault intraplate earthquake sequence. Tectonophysics 766, 151–166. https://doi.org/10.1016/j.tecto.2019.06.007.

Moss, R.E.S., Ross, Z.E., 2011. Probabilistic fault displacement hazard analysis for reverse faults. Bull. Seismol. Soc. Am. v. 101, 1542–1553. https://doi.org/10.1785/0120100248.

Murray, A.S., Thomsen, K.J., Masuda, N., Buylaert, J.P., Jain, M., 2012. Identifying well-bleached quartz using the different bleaching rates of quartz and feldspar luminescence signals. Radiat. Meas. 47, 688–695. https://doi.org/10.1016/j.radmeas.2012.05.006.

Nathan, S., Rattenbury, M., Suggate, R., (compilers), 2002. Geology of the Greymouth Area: Lower Hutt, New Zealand. Institute of Geological and Nuclear Sciences Geological Map 12, scale 1:250,000, 1 sheet plus 65 p.

Nicol, A., Van Dissen, R.J., 2002. Up-dip partitioning of displacement components on the oblique-slip Clarence Fault, New Zealand. J. Struct. Geol. 24, 1521–1535. https://doi.org/10.1016/S0191-8141(01)00141-9.

Nicol, A., Walsh, J., Berryman, K., Villamor, P., 2006. Interdependence of fault displacement rates and paleoearthquakes in an active rift. Geology 34, 865–868. https://doi.org/10.1130/G22335.1.

Ninis, D., Little, T.A., Van Dissen, R.J., Litchfield, N.J., Smith, E.G.C., Wang, N., Rieser, U., Henderson, C.M., 2013. Slip rate on the wellington fault, New Zealand, during the late quaternary: evidence for variable slip during the Holocene. Bull. Seismol. Soc. Am. 103, 559–579. https://doi.org/10.1785/0120120162.

Norris, R., Cooper, A., 2001. Late Quaternary slip rates and slip partitioning on the Alpine Fault, New Zealand. J. Struct. Geol. 23, 507–520. https://doi.org/10.1016/S0191-8141(00)00122-X.

Parsons, T., Field, E.H., Page, M.T., Milner, K., 2012. Possible earthquake rupture connections on mapped California Faults ranked by calculated coulomb linking stresses. Bull. Seismol. Soc. Am. 102, 2667–2676. https://doi.org/10.1785/0120110349.

Quigley, M., Van Dissen, R.J., Litchfield, N., Villamor, P., Duffy, B., Barrell, D., Furlong, K., Stahl, T., Bilderback, E., Noble, D., 2012. Surface rupture during the 2010 Mw 7.1 darfield(canterbury) earthquake: implications for fault rupture dynamics and seismic-hazard analysis. Geology 40, 55–58. https://doi.org/10.1130/G32528.1.

Quigley, M.C., Jiménez, A., Duffy, B., King, T.R., 2019. Physical and statistical behavior of multifault earthquakes: darfield earthquake case study, New Zealand. J. Geophys. Res. Solid Earth 124, 4788–4810. https://doi.org/10.1029/2019JB017508.

Reasenberg, P.A., Simpson, R.W., 1997. Response of Regional Seismicity to the Static Stress Change Produced by the Loma Prieta Earthquake: US Geological Survey Professional Paper.

Rockwell, T.K., Lindvall, S., Herzberg, M., Murbach, D., Dawson, T., Berger, G., 2000. Paleoseismology of the Johnson Valley, Kickapoo, and Homestead Valley faults: clustering of earthquakes in the Eastern California shear zone. Bull. Seismol. Soc. Am. 90, 1200–1236. https://doi.org/10.1785/0119990023.

Rodgers, D.W., Little, T.A., 2006. World's largest coseismic strike-slip offset: the 1855 rupture of the Wairarapa Fault, New Zealand, and implications for displacement/length scaling of continental earthquakes. J. Geophys. Res. Solid Earth 111, 1–19. https://doi.org/10.1029/2005JB004065.

Rother, H., 2006. Late Pleistocene Glacial Geology of the Hope-Waiau Valley System in North Canterbury. University of Canterbury, New Zealand, pp. 1–74.

Rother, H., Shulmeister, J., Rieser, U., 2010. Stratigraphy, optical dating chronology (IRSL) and depositional model of pre-LGM glacial deposits in the Hope Valley, New Zealand. Quat. Sci. Rev. 29, 576–592. https://doi.org/10.1016/j.quascirev.2009.11.001.

Rother, H., Shulmeister, J., Fink, D., Alexander, D., Bell, D., 2015. Surface exposure chronology of the Waimakariri glacial sequence in the Southern Alps of New Zealand: implications for MIS-2 ice extent and LGM glacial mass balance. Earth Planet. Sci. Lett. 429, 69–81. https://doi.org/10.1016/j.epsl.2015.07.033.

Rowan, A.V., Roberts, H.M., Jones, M.A., Duller, G.A.T., Covey-Crump, S.J., Brocklehurst, S.H., 2012. Optically stimulated luminescence dating of glaciofluvial sediments on the Canterbury Plains, South Island, New Zealand. Quat. Geochronol. 8, 10–22. https://doi.org/10.1016/j.quageo.2011.11.013.

Shulmeister, J., Thackray, G.D., Rittenour, T.M., Hyatt, O.M., 2018. Multiple glacial advances in the Rangitata Valley, South Island, New Zealand, imply roles for Southern Hemisphere westerlies and summer insolation in MIS 3 glacial advances. Quat. Res. (U. S.) 89, 375–393. https://doi.org/10.1017/qua.2017.108.

Shulmeister, J., Thackray, G.D., Rittenour, T.M., Fink, D., Patton, N.R., 2019. The timing and nature of the last glacial cycle in New Zealand. Quat. Sci. Rev. 206, 1–20. https://doi.org/10.1016/j.quascirev.2018.12.020.

Sohbati, R., Borella, J., Murray, A., Quigley, M., Buylaert, J.P., 2016. Optical dating of loessic hillslope sediments constrains timing of prehistoric rockfalls, Christchurch, New Zealand. J. Quat. Sci. 31, 678–690. https://doi.org/10.1002/jqs.2895.

Stahl, T., Quigley, M.C., Bebbington, M.S., 2016. Tectonic geomorphology of the Fox Peak and Forest Creek Faults, South Canterbury, New Zealand: slip-rates, segmentation and earthquake magnitudes. N. Z. J. Geol. Geophys. 59, 568–591. https://doi.org/10.1080/00288306.2016.1212908.

Stein, R.S., 1999. The role of stress transfer in earthquake occurrence. Nature 402, 605–609. https://doi.org/10.1038/45144.

Stein, R.S., Barka, A.A., Dieterich, J.H., 1997. Progressive failure on the North Anatolian fault since 1939 by earthquake stress triggering. Geophys. J. Int. 128, 594–604. https://doi.org/10.1111/j.1365-246X.1997.tb05321.x.

Stirling, M., McVerry, G., Gerstenberger, M., Litchfield, N., Van Dissen, R., Berryman, K., Barnes, P., Wallace, L., Villamor, P., Langridge, R.M., Lamarche, G., Nodder, S., Reyners, M., Bradley, B., et al., 2012. National Seismic Hazard Model for New Zealand: 2010 update. Bull. Seismol. Soc. Am. 102, 1514–1542. https://doi.org/10.1785/0120110170.

Sutherland, Eberhart-Phillips, Harris, Stern, et al., 2007. Do great earthquakes occur on the Alpine Fault in central South Island, New Zealand? A Continental Plate Boundary: Tectonics at South Island, New Zealand. In: Okaya, Stern, Davey (Eds.), In: Geophysical Monograph Series, 175. American Geophysical Union, pp. 235–251.

Toda, S., Stein, R.S., Reasenberg, P.A., Dieterich, J.H., Yoshida, A., 1998. Stress transferred by the 1995 M w = 6.9 Kobe, Japan, shock: effect on aftershocks and future earthquake probabilities. J. Geophys. Res. Solid Earth 103, 24543–24565. https://doi.org/10.1029/98JB00765.

Toda, S., Stein, R.S., Richards-Dinger, K., Bozkurt, S.B., 2005. Forecasting the evolution of seismicity in southern California: animations built on earthquake stress transfer. J. Geophys. Res. Solid Earth 110, 1–17. https://doi.org/10.1029/2004JB003415.

Van Dissen, R., Yeats, R., 1991. Hope fault, Jordan thrust, and uplift of the Seaward Kaikoura Range, New Zealand. Geology 19 (4), 393–396. https://doi.org/10.1130/0091-7613(1991)019<0393:HFJTAU>2.3.CO;2.

Vermeer, J.L., Quigley, M.C., Duffy, B.G., Langridge, R.M., Pettinga, J.R., 2021. Structure and kinematics of active faulting in the Hope-Kelly and Alpine Fault intersection zone, South Island, New Zealand. Tectonophysics 813, 228928. https://doi.org/10.1016/j.tecto.2021.228928.

Wallace, L., Beavan, J., McCaffrey, R., Berryman, K., Denys, P., 2007. Balancing the plate motion budget in the South Island, New Zealand using GPS, geological and seismological data. Geophys. J. Internat. 168 (1), 332–352. https://doi.org/10.1111/j.1365-246X.2006.03183.x.

Walters, R.J., Gregory, L.C., Wedmore, L.N.J., Craig, T.J., McCaffrey, K., Wilkinson, M., Chen, J., Li, Z., Elliott, J.R., Goodall, H., Iezzi, F., Livio, F., Michetti, A.M., Roberts, G., et al., 2018. Dual control of fault intersections on stop-start rupture in the 2016 Central Italy seismic sequence. Earth Planet. Sci. Lett. 500, 1–14. https://doi.org/10.1016/j.epsl.2018.07.043.

Wells, A., Yetton, M.D., Duncan, R.P., Stewart, G.H., 1999. Prehistoric dates of the most recent Alpine Fault earthquakes, New Zealand. Geology 27, 995–998. https://doi.org/10.1130/0091-7613(1999)027<0995:PDOTMR>2.3.CO;2.

Wesnousky, S.G., 2006. Predicting the endpoints of earthquake ruptures. Nature 444, 358–360. https://doi.org/10.1038/nature05275.

Yang, J.S., 1991. The Kakapo Fault — a major active dextral fault in the central North Canterbury - Buller regions of New Zealand. New Zealand J. Geol. Geophys. 34 (2), 137–143. https://doi.org/10.1080/00288306.1991.9514451.

Yetton, M.D., 1998. Progress in understanding the paleoseismicity of the central and northern Alpine Fault, Westland, New Zealand. N. Z. J. Geol. Geophys. 41, 475–483. https://doi.org/10.1080/00288306.1998.9514824.

Zachariasen, Berryman, Langridge, Prentice, Rymer, Stirling, Villamor, 2006. Timing of late Holocene surface rupture of the Wairau Fault, Marlborough, New Zealand. New Zealand J. Geol. Geophys. 49 (1), 159–174. https://doi.org/10.1080/00288306.2006.9515156.

Zechar, J.D., Frankel, K.L., 2009. Incorporating and reporting uncertainties in fault slip-rates. J. Geophys. Res. Solid Earth 114, 1–9. https://doi.org/10.1029/2009JB006325.

Zhan, Z., Jin, B., Wei, S., Graves, R.W., 2011a. Coulomb stress change sensitivity due to variability in mainshock source models and receiving fault parameters: a case study of the 2010-2011 Christchurch, New Zealand, earthquakes. Seismol. Res. Lett. 82, 800–814. https://doi.org/10.1785/gssrl.82.6.800.

Zielke, O., 2018. Earthquake recurrence and the resolution potential of tectono-geomorphic records. Bull. Seismol. Soc. Am. v. 108, 1399–1413. https://doi.org/10.1785/0120170241.

Zielke, O., Klinger, Y., Arrowsmith, J.R., 2015. Fault slip and earthquake recurrence along strike-slip faults - contributions of high-resolution geomorphic data. Tectonophysics 638, 43–62. https://doi.org/10.1016/j.tecto.2014.11.004.

Zinke, R., Hollingsworth, J., Dolan, J.F., 2014. Surface slip and off-fault deformation patterns in the 2013 M W 7.7 Balochistan, Pakistan earthquake: Implications for controls on the distribution of near-surface coseismic slip. Geochem. Geophys. Geosyst. 15, 5034–5050. https://doi.org/10.1002/2014GC005538.

Zinke, R.W., Dolan, J.F., Rhodes, E.J., Van Dissen, R., McGuire, C.P., 2017. Highly variable latest Pleistocene-Holocene incremental slip rates on the awatere Fault at Saxton River, South Island, New Zealand, revealed by lidar mapping and luminescence dating. Geophys. Res. Lett. 44, 11,301–11,310. https://doi.org/10.1002/2017GL075048.

Zinke, R.W., Dolan, J.F., Rhodes, E.J., Van Dissen, R.J., McGuire, C.P., Hatem, A.E., Brown, N.D., Langridge, R.M., 2019. Multimillennial incremental slip rate variability of the Clarence Fault at the Tophouse Road Site, Marlborough Fault System, New Zealand. Geophys. Res. Lett. 46, 717–725. https://doi.org/10.1029/2018GL080688.

Zinke, R.W., Dolan, J.F., Rhodes, E.J., Van Dissen, R.J., Hatem, A.E., McGuire, C.P., Brown, N.D., Grenader, J.R., 2021. Latest Pleistocene–Holocene incremental slip rates of the wairau fault: implications for long-distance and long-term coordination of faulting between North and South Island, New Zealand. Geochem. Geophys. Geosyst. 22, 1–16. https://doi.org/10.1029/2021GC009656.